Vibronic transitions in the alkali-metal (Li, Na, K, Rb) – alkaline-earth-metal (Ca, Sr) series: A systematic analysis of de-excitation mechanisms based on the graphical mapping of Frank-Condon integrals

Johann V. Pototschnig, Ralf Meyer, Andreas W. Hauser,* and Wolfgang E. Ernst†
Institute of Experimental Physics, Graz University of Technology, Petersgasse 16, A-8010 Graz, Austria
(Received 2 September 2016; revised manuscript received 4 November 2016; published 2 February 2017)

Research on ultracold molecules has seen a growing interest recently in the context of high-resolution spectroscopy and quantum computation. After forming weakly bound molecules from atoms in cold collisions, the preparation of molecules in low vibrational levels of the ground state is experimentally challenging, and typically achieved by population transfer using excited electronic states. Accurate potential energy surfaces are needed for a correct description of processes such as the coherent de-excitation from the highest and therefore weakly bound vibrational levels in the electronic ground state via couplings to electronically excited states. This paper is dedicated to the vibrational analysis of potentially relevant electronically excited states in the alkali-metal (Li, Na, K, Rb)– alkaline-earth metal (Ca,Sr) diatomic series. Graphical maps of Frank-Condon overlap integrals are presented for all molecules of the group. By comparison to overlap graphics produced for idealized potential surfaces, we judge the usability of the selected states for future experiments on laser-enhanced molecular formation from mixtures of quantum degenerate gases.

DOI: 10.1103/PhysRevA.95.022501

I. INTRODUCTION

The formation and trapping of molecules in the sub-microkelvin range has become a topical research branch in the past decade [1–6]. Ensembles of ultracold molecules have been suggested for the simulation of quantum systems [7–12], for quantum computation [13], or for controlled chemical reactions [14–16]. From a spectroscopic point of view, noise reduction and narrow linewidths allow precise measurements of fundamental physical properties and constants [17] such as the proton to electron mass ratio [18–20], the electron electric dipole moment [21,22] or the fine structure constant [23,24].

Due to limitations of direct techniques such as optical [25], buffer gas [26], or Stark [27] cooling, combinations of Feshbach resonance and photoassociation methods [4,28,29] have become standard techniques for the formation of molecules from pre-cooled atomic samples. Here, the group of alkali-alkaline earth diatomics stands out due to their permanent electric dipole moment in combination with a magnetic dipole moment in their $^2\Sigma^+$ ground state, which allows convenient manipulations with an external electric or magnetic field. Additionally, effective laser cooling and trapping techniques have been developed for the atoms involved [30,31].

Recent focus has been set on the ^{87}Rb ^{84}Sr molecule, for which a heteronuclear Feshbach scheme has been proposed [32]. On the experimental side, the simultaneous magneto-optical trapping of both elements and even combined Bose-Einstein condensates could be achieved [33,34]. The properties of alkali-alkaline earth diatomic molecules have also been studied by helium nanodroplet isolation spectroscopy [35,36] in our group [37–39]. In a series of combined experimental and computational studies [40,41] we identified several features of resonance enhanced multiphoton ionization (REMPI) spectra and matched them to computed excited electronic states. In a previous paper we analyzed the behavior of the lowest Σ^+ states of the doublet and the quartet multiplicity for different combinations of alkali-metal (*AK*) and alkaline-earth-metal (*AKE*) atoms, and studied the trends of molecular properties such as the dipole moment [42]. Reasonably large values of the latter are necessary to align molecules in optical lattices [43,44] or to control interactions with an external microwave field [4,11,45]. To the knowledge of the authors only two other molecules of our set besides RbSr have been studied experimentally, namely LiCa [37,46,47] and RbCa [41]. On the purely theoretical side, several publications can be found for LiCa [18,42,48–52], NaCa [42,44,53], KCa [42,44] RbCa [41,42,44], LiSr [18,42,49–53], NaSr [42,44,53], KSr [42,44,53], and RbSr [40,42,44,53–55].

Among them, Chen *et al.* dedicated a recent paper [54] to the detailed investigation of rovibrational levels in the electronic ground state and three electronically excited states. In this work, we aim at the generalization of these recently proposed de-excitation schemes to our selection of *AK*-*AKE* diatomics. In the first part of the manuscript we focus on the calculation of potential energy surfaces of the first few electronically excited, experimentally relevant states. We employ various *ab initio* methods, discuss deviations in the curvatures and the relative energy positions, and analyze their consequences for a quantitative analysis of vibronic spectra. This is followed by the calculation of Franck-Condon factors and Einstein *A* coefficients to study potential mechanisms for the transfer of initially formed, weakly bound molecules to the rovibrational ground state.

The article is organized as follows. Section II gives an outline of our computational approach, presents our potential

*andreas.w.hauser@gmail.com
†wolfgang.ernst@tugraz.at

energy surface (PES) fitting and interpolation technique, and contains details of the numerical evaluation of rovibrational states. Three different methods, equation-of-motion coupled cluster, multireference configuration interaction, and multireference perturbation theory are applied in order to obtain PES and transition dipole moments for a selection of relevant states. A brief overview of our spin-orbit coupling approach is given. In Sec. III we analyze the PES of the $X\,^2\Sigma^+$ ground state, the second and third $^2\Sigma^+$ electronically excited state, the first and second $^2\Pi$ electronically excited state, as well as two quartet states ($1\,^4\Sigma^+$, $1\,^4\Pi$) for all molecules of the M_{AK}-Sr and M_{AK}-Ca series. All of the electronically excited states correspond to single $s \rightarrow p$ atomic excitations in the dissociation limit. Our findings are then compared to previous computations and experimental results where possible. Section IV starts with a brief discussion of effects of potential shapes on the graphical matrix representation of the Franck-Condon factors. The insights gained from these studies are then used for the interpretation of the relevant transitions in the *AK-AKE* diatomics. We comment on potential de-excitation mechanisms involving the electronic states of interest. Special focus is given to the process suggested in Ref. [54] for the RbSr molecule, which involves an excitation from the $X^2\Sigma^+$ ground state into the $2\ \Omega = \frac{1}{2}$ electronically excited state (corresponding to $1\,^2\Pi$). The original scheme is then transferred onto the other *AK-AKE* combinations and consequently re-evaluated for experimental relevance. Keeping in mind the experimentally accessible range, we then give a few alternatives based on excitations to other electronically excited states.

II. THEORETICAL ASPECTS

A. *Ab initio* methods

A first data set is derived from multiconfigurational self-consistent field calculations (MCSCF [56,57]), followed by either multireference configuration interaction including Davidson correction (MRCI [58,59]) or multireference perturbation theory (CASPT2 [60]), both of second order. For the sake of a direct comparison, we further apply equation-of-motion coupled cluster theory (EOM-CCSD [61]). In the MRCI and CASPT2 approach only the three valence electrons were included in the active space. The core orbitals were optimized in the preceding MCSCF treatment, but kept doubly occupied. Missing correlation with the core electrons is accounted for by core polarization potentials (CPPs) as introduced by Müller and Meyer [62]. The corresponding parameters can be found in Ref. [42], where their importance for a correct description of the static dipole moment was demonstrated. Typically, the permanent electric dipole moment (PEDM) is overestimated if core polarization is neglected [63]. The active spaces in the MCSCF and subsequent computations are kept the same for all molecules and are constructed according to the various elements and their effective core potentials.

For Li and Na we used the all electron aug-cc-pCV5Z basis set of the Peterson group [64]. For K, Rb, Ca, and Sr we combined the effective core potentials of Lim *et al.* [65–67] with the corresponding basis sets for K and Rb [68]. For Sr and Ca we use the cc-pCV5Z-PP basis sets of the Peterson group [69]. Note that basis functions with an orbital angular momentum quantum number larger than 5 are neglected due to internal program limitations if CPPs are used. The same basis functions were excluded in the EOM-CCSD computation for an unbiased comparison of the methods [70]. In the MCSCF and subsequent calculations, the two g functions with the highest exponents were removed from the Na basis set to avoid convergence issues at large internuclear separations.

B. Inclusion of spin-orbit coupling

Spin-orbit coupling is taken into consideration for the heavier diatomic molecules (KCa, RbCa, KSr, RbSr) due to the significant energy splitting which occurs in these cases. We use Hund's case (a) eigenstates as basis set for the matrix representation of effective spin-orbit Hamiltonians [55] and diagonalize these matrices to obtain the energy corrections. The three coupling constants required for the evaluation of matrix elements can be derived from atomic spin-orbit splitting [71,72]. In this case a spin-orbit coupling parameter given by the atomic spin-orbit splitting is used for all distances. The distance dependence of the coupling parameter can be considered using the Breit-Pauli approximation, which was done, for example, for RbSr [40] or SrYb [73]. In this work we used the MOLPRO software package [74] for this purpose and passed the distance-dependent matrix element to the DUO software package [75].

C. Choice of states

The focus of this study lies on the lowest electronic states of the *AK-AKE* molecules, which comprise the ground state and the states asymptotically approaching the lowest ^2P and ^3P excitation of the *AK* and *AKE* atom, respectively. In the Hund's case (a) notation, this results in five states with doublet multiplicity and two states with quartet multiplicity, which have been selected due to their computational feasibility and their potential relevance in future experiments. In the MCSCF and MRCI computations higher electronically excited states had to be included in order to obtain smooth and converged potential energy curves. The doublet and quartet states are treated together via state-averaged MCSCF. In the case of the CCSD calculations, three different restricted open-shell Hartree-Fock (ROHF) reference wave functions are employed: The ground state ($X^2\Sigma^+$) is obtained from a CCSD calculation based on a ROHF reference state, while the excited states in the doublet manifold are calculated with EOM-CCSD. The quartet states are determined by separate CCSD computations with appropriate ROHF references. These excited quartet states ($1\,^4\Sigma^+$, $1\,^4\Pi$) have the same asymptote as either the $2\,^2\Sigma^+$ and $1\,^2\Pi$ or the $3\,^2\Sigma^+$ and $2\,^2\Pi$ states, depending on which combination of atoms is considered. Due to the different treatment of both multiplicities (EOM-CCSD versus CCSD), the asymptotic energies differ by about 516 cm^{-1} for Ca and about 540 cm^{-1} for Sr at 20 Å. This error of about 5% was corrected by *ad hoc* shifting of the quartet states. In all other cases, the asymptotic values of the transition energies differ by less than 1% from the tabulated values in the NIST database [71]. The similarity of the three *ab initio* methods for the lower states is demonstrated in Fig. 1 for NaSr. Similar

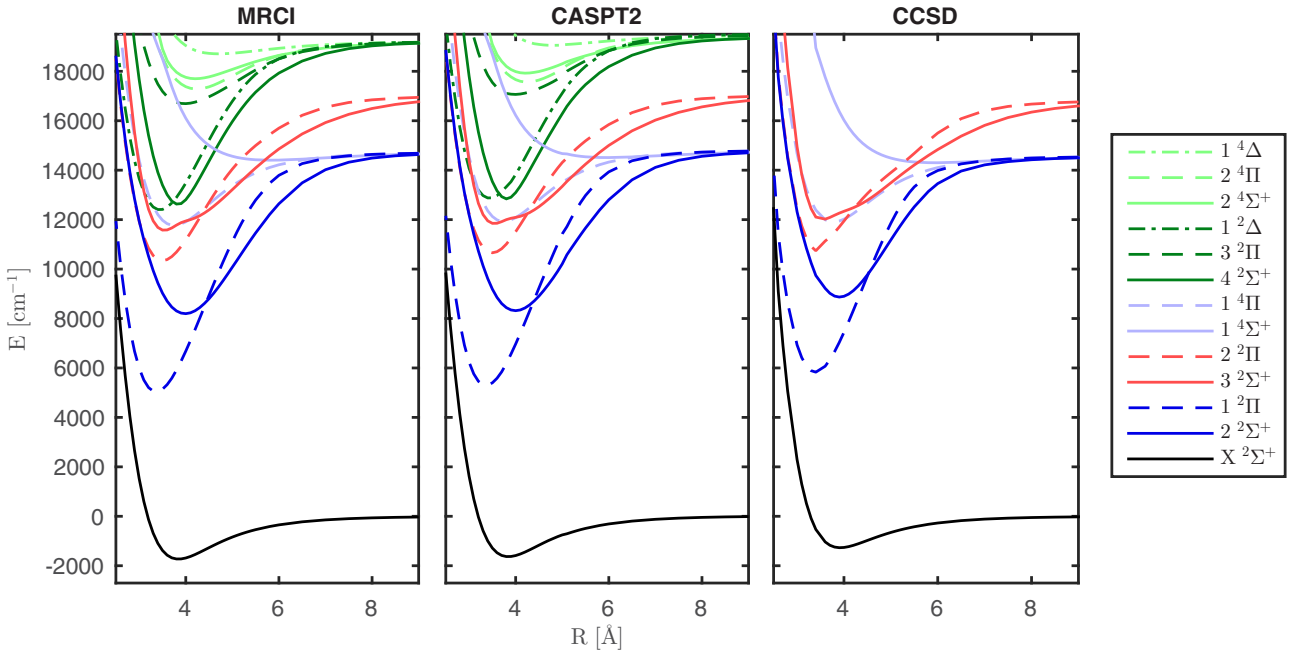

FIG. 1. Potential energy curves for NaSr obtained by different methods.

figures for other *AK-AKE* combinations are included in the Supplemental Material [76]. For higher states (green curves in the figure, above the lowest seven PECs), the results obtained with different methods start to deviate from each other even qualitatively. In particular, the EOM-CCSD results seem to be problematic, as has already been indicated in Ref. [55]. Therefore, higher states are excluded from our analysis.

All MRCI and CASPT2 calculations are carried out with the MOLPRO software package [58,60,74,77,78]. For the EOM-CCSD computations we use the CFOUR suite of programs [61,79].

D. Model potential

In Sec. IV the *ab initio* data will be used for a vibrational analysis. A Morse/Long-Range (MLR) potential is fitted to the data points using the program BETAFIT 2.1 [80]. The MLR potential has the following functional form:

$$V(r) = D_e\left[1 - \frac{u_{LR}(r)}{u_{LR}(r_e)}e^{-\beta(r)y^{eq}(r,6)}\right]^2, \quad (1)$$

in which D_e is the potential depth, r_e is the equilibrium distance, and $y^{eq}(r,p)$ is a radial variable of the form,

$$y^{eq}(r,p) = \frac{r^p - r_e^p}{r^p + r_e^p}. \quad (2)$$

The long-range potential $u_{LR}(r)$ is expressed as an inverse power series using the parameters calculated by Jiang *et al.* [81]:

$$u_{LR}(r) = \frac{C_6}{r^6} + \frac{C_8}{r^8} + \frac{C_{10}}{r^{10}}. \quad (3)$$

These parameters were transformed with the eigenvector of the effective Hamiltonian if the spin-orbit coupling was included according to Sec. II B. The exponent coefficient function $\beta(r)$ introduces an additional flexibility to the Morse part of the potential:

$$\beta(r) = y^{eq}(r,6)\beta_\infty + [1 - y^{eq}(r,6)]\sum_{i=0}^{N_\beta}\beta_i y^{eq}(r,4)^i. \quad (4)$$

The asymptotic value of the exponent function, denoted as β_∞, is required to have the value $\beta_\infty = \ln[2D_e/u_{LR}(r_e)]$. We use a total of 10 expansion coefficients β_i ($N_\beta = 10$). Further details on the model potential and the fitting procedure can be found in the BETAFIT manual [80].

The transition dipole moment (TDM) data were interpolated by cubic Hermite splines due to the oscillating behavior observed for simple cubic splines. For the long-range region the data were extrapolated to reproduce the asymptotic TDM, which was calculated from the outermost *ab initio* points.

E. Computation of rovibrational states

The calculation of the rovibrational wave functions from the fitted and interpolated potentials in the limit of zero spin-orbit coupling is done with the LEVEl 8.0 program [82]. It determines the eigenvalues and eigenfunctions of the nuclear Schrödinger equation,

$$-\frac{\hbar^2}{2\mu}\frac{d^2\Psi_{v,J}(r)}{dr^2} + V_J(r)\Psi_{v,J}(r) = E_{v,J}\Psi_{v,J}(r), \quad (5)$$

for a given potential energy surface. The selection of isotopes (^{7}Li, ^{23}Na, ^{39}K, ^{87}Rb, ^{40}Ca, and ^{84}Sr) enters the calculation through the reduced mass μ. The Franck-Condon (FC) factors,

$$f_{v''\to v'} = |\langle g, v'', J''|e, v', J'\rangle|^2, \quad (6)$$

for the $J'' = 0 \to J' = 1$ transitions were calculated using this program as well as the Einstein A coefficients using distance-dependent transition dipole moments.

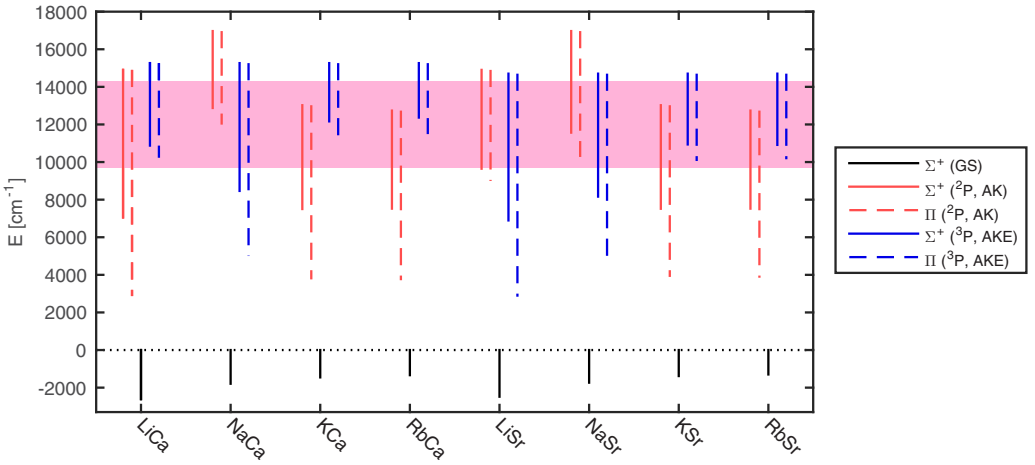

FIG. 2. Spectroscopic regions with vibronic states for the different molecules. The zero axis corresponds to the dissociation limit of the ground state. The marked region corresponds to energies that can be addressed by a Ti:sapphire laser.

The program performs an integration over a radial grid; the accuracy of the results shows a dependence on the grid spacing. A step size of $r_H = 0.002$ Å was used which is even smaller than the recommendation of the particle-in-a-box approximation given in the manual of LEVEL 8.0 [82]. The starting points of the numerical grids were selected for the different molecules as follows: $r_{min} = 2.4$ Å for LiCa, NaCa, and KCa, $r_{min} = 2.25$ Å for RbCa and RbSr, $r_{min} = 2.1$ Å for LiSr, NaSr, and KSr with an end point fixed at $r_{max} = 100$ Å. The same grid was used for the Hund's case (c) potentials with the exception of larger starting radii for the two most weakly bound states.

For the sake of a direct comparison, the Einstein A coefficients were also determined by the DUO software package [75]. In this case the Hund's case (a) potential energy curves fitted by BETAFIT were passed on to the program with a grid spacing of 0.1 Å. About 40 points of our *ab initio* transition dipole moments were also fed to the program to allow for a calculation of Einstein A factors. Additionally, the distance-dependent spin-orbit coupling matrix elements were used to account for spin-orbit coupling. In the DUO calculations the same intervals were used for the numerical grid with 5000 grid points. Note that due to the intermediate character of the numerically evaluated eigenstates neither Hund's case (a) nor Hund's case (c) is fully appropriate. The identification of the obtained states in either picture is based on the leading coefficients in a linear expansion. In ambivalent cases (i.e., states with identical quantum numbers) the state of lowest energy is picked for the graphical illustration.

III. PES DISCUSSION

Before going into details of the calculated PES, we start with an overall presentation of the energy regions spanned by the electronically excited states selected in this article. Figure 2 serves as guidance to experimentalists, comparing the spectral range of the relevant Σ^+ and Π band systems of each *AK-AKE* molecule of the series to the energy range covered by a Ti:sapphire laser system. The length of each vertical line in the figure corresponds to the MRCI dissociation energy of a given electronic state, while its upper position is determined by the known atomic excitation energy. As can be seen, all states selected in this study show at least a partial overlap with the energy range of this standard device. Regarding the simultaneous accessibility of vibrational bands in all four electronically excited states, the molecules LiSr and LiCa seem best suited, followed by NaSr, KSr, and RbSr. Ti:sapphire lasers have been used extensively for the study and manipulation of *AK* diatomics produced from ultracold atoms by photoassociation. Examples are LiCs (≈10 600 cm^{-1}) [83], RbCs (≈11 200 cm^{-1}) [84], NaCs (≈11 700 cm^{-1}) [85,86], KRb (≈12 500 cm^{-1}) [87–90], RbYb (≈12 500 cm^{-1}) [91], and LiRb (≈12 500–12 800 cm^{-1}) [92,93]. Alternatively, diode lasers were used for Cs_2 (≈11 700 cm^{-1}) [29] and LiK (≈13 000 cm^{-1}) [94]. Besides photoassociation, lasers have also been used to transfer ultracold molecules from weakly to strongly bound vibrational states via stimulated Raman adiabatic passage (STIRAP) [95]. Again, applications of Ti:sapphire lasers could be found for Rb_2 (≈9800 cm^{-1}) [96] and KRb (≈9800 cm^{-1}) [97,98], but also stabilized diode lasers in the case of Cs_2 (≈8800 and 9900 cm^{-1}) [99,100], Rb_2 (≈10 000 cm^{-1}) [96], and KRb (≈9300 and 15 600 cm^{-1}) [90,97,98].

Photoassociation might also work for this class of molecules (e.g., for K-M_{AKE} at about 13 000 cm^{-1}or for Rb-M_{AKE} at about 12 500 cm^{-1}), although here the excited doublet states are more strongly bound than the ground states, which probably limits the efficiency of such an approach. STIRAP schemes, in contrast, often make use of lower lying vibrational levels. In order to predict the feasibility of such schemes and to select potential candidate states more detailed PES information is required. An adequate description of the long-range part is crucial for predictions concerning photoassociation or STIRAP transfer processes where the atoms are initially separated by large distances. The main long-range behavior of such molecules is given by r^{-6} for heteronuclear molecules, in contrast to homonuclear molecules which show a r^{-3} dependency for the resonant dipole interaction of excited states [1]. The related dispersion coefficients can be derived from atomic properties as was done by Jiang *et al.* [81] for this class of molecules.

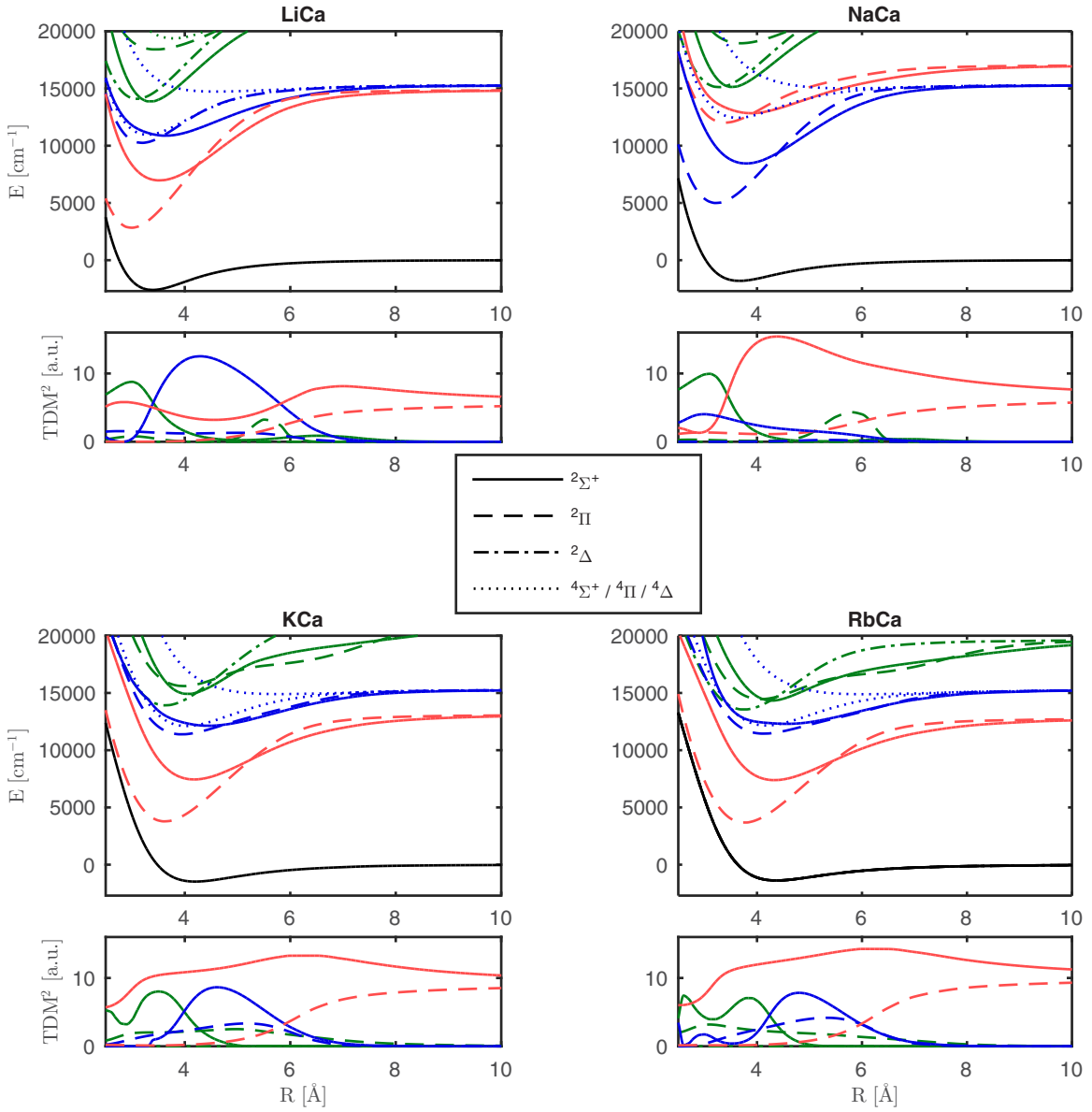

FIG. 3. PECs for the alkali-metal–(Li, Na, K, Rb) Ca series as determined by MRCI up to 20 000 cm^{-1}.

A. Potential curves and transition dipole moments

In Fig. 3 the potential energy curves of the M_{AK}-Ca series are shown together with the transition dipole moments between the ground states and the respective excited states. Figure 4 displays the same for the M_{AK}-Sr series.

The features of the M_{AK}-Ca and M_{AK}-Sr molecules are very similar. There is an energetic proximity of the 4*s*-4*p* transition of Ca (near 15 200 cm^{-1}), the 5*s*-5*p* transition of Sr (near 14 700 cm^{-1}), and the 2*s*-2*p* transition of Li (near 14 900 cm^{-1}). Therefore, the asymptotes are hardly distinguishable in Figs. 3 and 4 for LiCa and LiSr. For the other *AK* atoms the order is independent of the *AKE* atom and the asymptotes are clearly separated in the depictions. The first transition of K and Rb are below the *AKE* transitions, the opposite is observed for Na. The proximity of the asymptotes in the Li-M_{AKE} molecules also leads to a large overlap of vibrational bands in the $2/3\ ^2\Sigma^+$ and $1/2^2\Pi$ electronic states. Irrespectively of the asymptotes, the $2\ ^2\Sigma^+$ and $1\ ^2\Pi$ have larger dissociation energies than the next state of the same symmetry. Regarding the three lowest Π states (two doublet and one quartet state), another trend is obvious: The PES minima are typically bound at shorter internuclear distances than the ground-state minimum with significantly larger potential depths. The Σ^+ states, on the other hand, show similar distances except for the lowest quartet state, which is bound at a much larger distance. Another feature shown by all molecules is an avoided crossing between the $3\ ^2\Sigma^+$ and $4\ ^2\Sigma^+$ states. This results in an atypical form of the potentials involved. Due to the closeness of the avoided crossing and the minima the extraction of PES parameters based on Morse fits is problematic. In all cases, the excited state PES shows much more pronounced minima, with the exception of the $1^4\Sigma^+$ state. In particular, the $^2\Pi$ states are more strongly bound than other states, with dissociation energies up to 12 000 cm^{-1}.

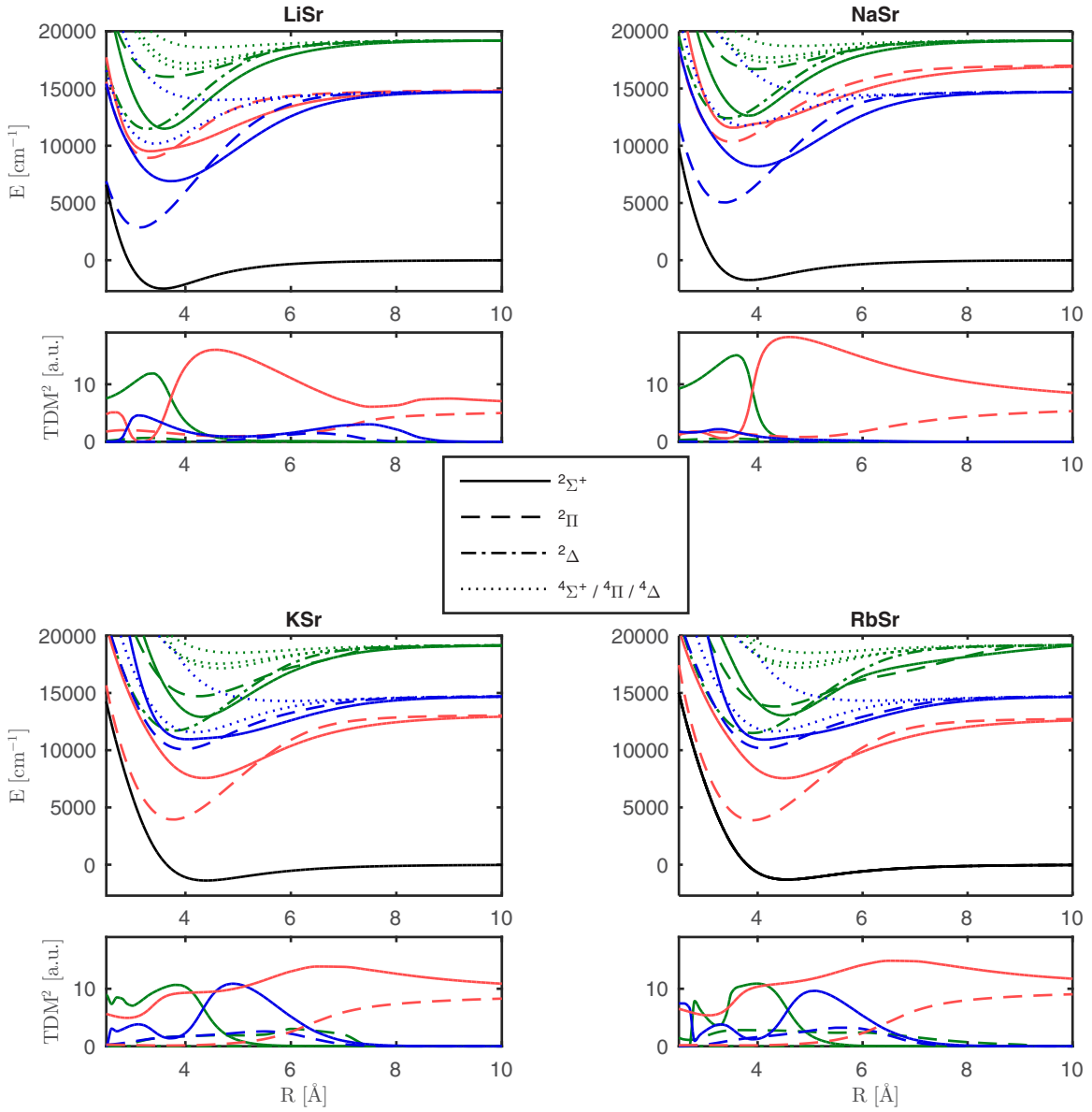

FIG. 4. PECs for the alkali-metal (Li, Na, K, Rb)–Sr series as determined by MRCI up to 20000 cm^{-1}.

Regarding the dependence of the transition dipole moment on the internuclear distance we find an insensitivity for the $2\,^2\Sigma^+ \leftarrow X\,^2\Sigma^+$ transition in the K/Rb-*AKE* molecules, which is barely affected by moderate geometry changes, see red (light gray) solid line in the TDM subplots. A similar behavior is observed for LiCa, although there seems to be an intensity borrowing effect starting at 6 Å. The high value of the TDM at large distances for these states is in agreement with the atomic behavior, as they correspond to the ^2P state of the *AK* atom, which shows a large transition probability. The corresponding atomic line strengths S_{ik} for the $^2P_{\frac{3}{2}}$ are 22.0, 24.9, 33.8, and 35.7 $e^2a_0^2$ as listed in the NIST database [71] for Li, Na, K, and Rb, respectively. Taking the degeneracy into account (S_{ik}/g_k), values of 5.5, 6.2, 8.5, and 8.9 $e^2a_0^2$ are obtained. The computed values of 5.7, 6.8, 9.2, and 10.0 $e^2a_0^2$ agree well with these numbers. The second transition related to this asymptote, the $1\,^2\Pi \leftarrow X\,^2\Sigma^+$ transition, shows about the same TDM at large distances, but decays faster and is already reduced to about half its value at 6 Å. Note that in the case of NaCa, NaSr, and LiSr, the $3\,^2\Sigma^+$ and $2\,^2\Pi$ states show this behavior and correspond to the lowest excitation of the *AK* atom. For the lighter *AK* atoms, Li and Na, the other excited states show a small transition dipole moment, while for the heavier atoms also the $3\,^2\Sigma^+$ state, which corresponds to the ^3P asymptotes, has a significant transition dipole moment at typical bond distances. This agrees with the general trend that excitations into the Π states possess smaller dipole transition moments when directly compared to the Σ^+ states. Another general characteristic appearing in the TDM plots is an intensity-borrowing effect occurring for the second and third Σ^+ state in the range of their avoided crossing.

The above mentioned features of the PES are of relevance in the follow-up analysis of vibrational levels based on the Franck-Condon factors. The strongest influence on low vibrational levels stems from variations in the equilibrium distances, although smaller than 0.6 Å for the doublet states of each molecule, followed by curvature differences and

anharmonicity effects. In contrast, the Franck-Condon factors of the highest vibrational levels are most strongly affected by the different long-range behavior. An r^{-6} dependence is expected to be dominant for all states. The corresponding dispersion coefficients for the *AK-AKE* molecules are provided in Ref. [81]. Typically, the ground states show the smallest C_6 coefficients, which is correlated to the common feature of smallest dissociation energies for the ground states in comparison to the first few electronically excited states.

B. Spectroscopic parameters

In this part we present the spectroscopic data for the Hund's case (a) PES depicted in Sec. III A in tabular form and compare our results to experimental measurements where possible. To the knowledge of the authors, experimental data can only be found for the molecules LiCa, RbCa, and RbSr. For this reason we included the corresponding tables here (Table I–III), while data for the remaining combinations can be found in the Supplemental Material [76]. The parameters were determined for the following choice of isotopes: ^{7}Li, ^{23}Na, ^{39}K, ^{87}Rb, ^{40}Ca, and ^{84}Sr. Values for T_0, i.e., the energies for the $0 \leftarrow 0$ vibrational transitions between the ground and the electronically exited states, are calculated after the asymptotic correction of the *ab initio* data according to the NIST atomic level database [71]. The correction for the lowest seven states is less than 70 cm^{-1} for the MRCI results and less than 150 cm^{-1} for the other methods with the exception of the quartet states determined by CCSD. For higher states the deviation can amount up to 3000 cm^{-1}, which explains the unreliability for the 4 $^2\Sigma^+$ and 3 $^2\Pi$ states in the tables. The theoretical approach of this work is the same as in our earlier work [42]. Slight differences appear because we used 20 Å as the asymptotic value, increased the active space for selected molecules, and used the isotopes mentioned above instead of mean atomic masses.

Experimentally, LiCa is the best studied molecule of our set with the most accurate data which is listed alongside theoretical results in Table I. The dissociation energy of the ground state was determined by Stein *et al.* [47] and our current value agrees now better than the one provided earlier [37]. This work is mainly concerned with the states belonging to the three lowest asymptotes. Of these, only the 2 $^2\Sigma^+$ state has been investigated in LiCa. Here, the difference between the experimental and the MRCI transition energies lies in the range of about 50 cm^{-1}. Two higher states have been added to the table (4 $^2\Sigma^+$ and 3 $^2\Pi$) which differ in the transition energy by about 1000 cm^{-1}. This large deviation is probably related to the difficulty describing the ^3D asymptote of the Ca atom. We note that in our earlier work [37] a modified, molecule-specific combination of ECP and basis set had been chosen to obtain a better agreement for these states. For RbCa there is only one value for the states of interest in this work. The experimental and theoretical transition energies of the 3 $^2\Sigma^+$ state are listed in Table II and differ by about 500 cm^{-1}. This difference might be partly due to the limited laser range in the experiment. The values for two higher states (4 $^2\Sigma^+$/ 3 $^2\Pi$), which approach the ^2D state of Rb asymptotically, are also listed in Table II. The difference between the experimental and MRCI results is in these cases about 200 cm^{-1}. For RbSr, a roughly estimated experimental value of the vibrational constant is in agreement with the MRCI result of this work (see Table III). The T_0 value of the 3 $^2\Sigma^+$ state of the same molecule only differs by about 20 cm^{-1} from the experimental estimate. For the 2$^2\Pi$ state the difference is larger, but in this case the experimental features occur close to the end of the laser scan range. Two higher states with a ^3D (Sr) asymptote were included in Table III. In this case, the transition energy differs by about 700 cm^{-1}. Regarding the seven lowest states considered in the vibrational analysis, we expect deviations of about 100 cm^{-1} in absolute position for those vibrational levels close to the potential minimum and less for levels close to the asymptote. Therefore, a reliable one-to-one assignment of vibrational quantum numbers to features of vibrationally resolved experimental spectra is not yet possible.

With respect to overall features of the PES involved, the following trends have been observed for the different *ab initio* methods. In most cases, the MRCI potentials show the largest potential depth while the CCSD results show the smallest one. The CASPT2 results as well as nearly all literature values lie between these two extremes. MRCI and CASPT2 results agree better, which is expected since both are using the same multiconfigurational reference. The difference between the MRCI and CCSD results stems in part from the missing static correlation energy in the CC expansion. For all eight molecules, the 1$^2\Pi$ state has the largest dissociation energy ranging from 12017 to 8890 cm^{-1} and the smallest bond distance with values between 3.0 and 3.9 Å. These values as well as the following ones refer to the results obtained by the MRCI approach. The smallest bond energies were obtained for the 1$^4\Sigma^+$ state with values between 716 and 251 cm^{-1}. The equilibrium positions are the largest for this state and vary from 4.6 to 6.1 Å. Harmonic frequencies vary between 295 and 17 cm^{-1}, decreasing from LiCa to RbSr. The asymmetry parameter ($\omega_s x_e$) is correlated with the magnitude of the frequencies but about two orders of magnitude smaller. The ground state has a positive dipole moment (i.e., pointing from the *AKE* to the *AK* atom), while the 1$^4\Sigma^+$ lowest quartet state shows a negative value as discussed in Ref. [42]. Another trend is that the 1$^2\Pi$ and 2$^2\Pi$ states always have positive dipole moments with the exception of LiSr. The latter molecule also has the smallest permanent electric dipole moment in the ground state, and the difference of electronegativity shows the opposite sign compared to the other molecules (see Ref. [42] for details).

C. SO-corrected PES for the heavy *AK-AKE* diatomics

The spin-orbit corrected PES are plotted in Fig. 5 together with their corresponding transition dipole moments as a function of internuclear distance. Only the two lowest asymptotes are included in the graphics, with the *AKE*-related asymptote already showing a high density of states. We distinguish them by their total angular momentum projection quantum number Ω, which can take the values 1/2, 3/2, and 5/2. This last value of 5/2 stems from a Π state of quartet multiplicity which approaches the asymptote of the *s-p* transition in the *AKE* atom. Spin-orbit coupling introduces a whole series of additional avoided crossings in the PES structure, which leads to a more complex dependence of dipole transition moments.

TABLE I. Parameters for the electronically excited states of LiCa, obtained with the MRCI, CASPT2, and CCSD approaches. Results from previous publications are also listed.

State	Ref.	D_e(cm^{-1})	r_e(Å)	ω_e(cm^{-1})	$\omega_e x_e$(cm^{-1})	μ_e(D)[102]	T_0(cm^{-1})
$X\,^2\Sigma^+$	MRCI	2595	3.391	198.0	3.76	1.12	
	CASPT2	2545	3.390	197.9	3.85	0.99	
	CCSD	2211	3.345	206.8	4.83		
	[47]^{exp}	2605.3(100)	3.35582(10)	202.2386			
	[46]^{exp}		3.3796(11)[b]	195.2 [c]			
	[37]	2883	3.342	202.6			
	[52]	2097	3.400	191			
	[50]	2258	3.395	197.6		1.099 [d]	
	[49]	2607	3.364	207.1		1.12	
	[48]	2355	3.296	196.1	4.15		
$1\,^2\Pi$	MRCI	12 017	2.990	295.0	1.81	0.59	5531
	CASPT2	11 912	2.998	293.3	1.80	0.74	5585
	CCSD	11 180	2.980	282.6	1.79		5974
	[37]	12 630	2.948	283.5			5147[a]
	[52]	11 225	2.985	306			5882[a]
	[46]		3.052	286			6028[a]
	[48]		2.862	307.7	1.71		5520
$2\,^2\Sigma^+$	MRCI	7878	3.518	204.7	1.33	−3.40	9625
	CASPT2	7797	3.521	202.6	1.32	−3.52	9655
	CCSD	7537	3.501	240.8	1.92		9596
	[47]^{exp}	7937(10)	3.48514(3)	202.126(7)			9572.0483(108)[a]
	[37]	8360	3.503	201.7			9461[a]
	[52]	7280	3.562	196			9703[a]
	[46]		3.634	192			9138[a]
	[48]		3.423	220.6	1.33		9566
$2\,^2\Pi$	MRCI	5009	3.187	245.9	3.02	4.71	12 873
	CASPT2	4843	3.193	239.5	2.96	4.15	12 986
	CCSD	5002	3.153	257.0	3.30		12 498
	[37]	5771	3.127	257.0			11 990[a]
	[52]	3759	3.199	240			13 480[a]
	[46]		3.346	206			13 825[a]
	[48]		2.990	276.6	3.36		12 056
$3\,^2\Sigma^+$	MRCI	4379	3.633	149.9	1.28	2.10	13 456
	CASPT2	4342	3.647	153.0	1.35	1.99	13 444
	CCSD	3909	3.218	164.9	1.74		13 545
	[37]	4999	3.199	171.0			12 793[a]
	[52]	3572	3.670	164			13 745[a]
$1\,^4\Pi$	MRCI	4299	3.294	217.6	2.75	1.77	13 569
	CASPT2	4246	3.293	218.1	2.80	1.84	13 572
	CCSD	4121	3.246	221.9	2.99		13 361
	[37]	4704	3.221	223.0			13 050[a]
	[52]	3721	3.318	208			13 604[a]
	[48]		3.105	243.3	3.23		13 193
$1\,^4\Sigma^+$	MRCI	530	4.592	56.8	1.52	−4.66	17 258
	CASPT2	501	4.607	54.8	1.50	−4.88	17 236
	CCSD	445	4.159	52.7	1.56		16 953
	[37]	608	4.325	67.0			17 144[a]
	[52]	265	5.008	29.6			17 013[a]
$3\,^2\Pi$	MRCI	4640	3.447	163.6	1.44	−4.31	18 295
	CASPT2	4545	3.431	162.1	1.45	−4.92	18 339
	CCSD	8337	3.242	217.8	1.42		14 237
	[37]^{exp}			134(51)			19 334(42)[a]
	[46]^{exp}		3.5451(36)	144.5			19 285.8[a]
	[37]	4119	3.486	152.0			19 444[a]
	[48]		3.456	150.1	1.46		19 099
$4\,^2\Sigma^+$	MRCI	9175	3.353	287.6	2.25	0.55	13 822
	CASPT2	9110	3.332	290.3	2.31	−0.19	13 838
	CCSD	8940	3.319	387.1	4.19		13 718

TABLE I. (*Continued*.)

State	Ref.	D_e(cm^{-1})	r_e(Å)	ω_e(cm^{-1})	$\omega_e x_e$(cm^{-1})	μ_e(D)[102]	T_0(cm^{-1})
	[47][exp]	7701(10)	3.425	287.84(2)			15 282.180(5)
	[37][exp]			288(7)			15 340(8)[a]
	[46][exp]		3.3699(37)[b]	284.5[c]			15 237.6[a]
	[37]	8274	3.398	270.0			15 277[a]
	[48]		3.310	291.7	2.75		14 756

[exp], experimental results.
[a] T_e.
[b] r_0.
[c] $\Delta G_{1/2}$.
[d] μ_0.

TABLE II. Parameters for the electronically excited states of RbCa, obtained with the MRCI, CASPT2, and CCSD approaches. Results from previous publications are also listed.

State	Ref.	D_e(cm^{-1})	r_e(Å)	ω_e(cm^{-1})	$\omega_e x_e$(cm^{-1})	μ_e(D) [102]	T_0(cm^{-1})
$X^2\Sigma^+$	MRCI	1350	4.374	56.9	0.60	2.26	
	CASPT2	1304	4.382	55.9	0.60	1.97	
	CCSD	775	4.582	44.0	0.62		
	[41]	1406	4.37	58			
	[44]	921	4.53	49		1.75	
$1\,^2\Pi$	MRCI	9038	3.756	106.2	0.31	6.93	5074
	CASPT2	8933	3.757	106.1	0.32	6.98	5134
	CCSD	7802	3.791	104.9	0.35		5741
	[41]	9175	3.75	108			4772
$2\,^2\Sigma^+$	MRCI	5330	4.335	77.8	0.28	2.43	8768
	CASPT2	5257	4.335	77.7	0.29	2.10	8795
	CCSD	4487	4.352	77.4	0.33		9043
	[41]	5446	4.34	78			8487
$2\,^2\Pi$	MRCI	3783	4.125	70.4	0.33	5.99	12 837
	CASPT2	3643	4.143	68.0	0.32	3.33	12 930
	CCSD	2715	4.225	63.3	0.37		13 333
	[41]	4156	4.02	79			12 110
$3\,^2\Sigma^+$	MRCI	2931	4.566	45.5	0.18	4.33	13 676
	CASPT2	2926	4.600	48.2	0.20	3.22	13 637
	CCSD	1852	4.122	44.8	0.27		14 187
	[41][exp]						≈13 100
	[41]	3367	4.02	62			12 891
$1\,^4\Pi$	MRCI	3054	4.172	74.3	0.45	5.47	13 568
	CASPT2	3031	4.176	74.8	0.46	5.37	13 546
	CCSD	2587	4.210	71.4	0.49		13 465
	[41]	3220	4.13	77			13 045
$1\,^4\Sigma^+$	MRCI	331	6.043	18.8	0.27	−2.22	16 263
	CASPT2	324	6.022	18.8	0.27	−2.28	16 225
	CCSD	240	6.168	16.6	0.29		15 785
	[41]	336	5.98	19			15 901
$3\,^2\Pi$	MRCI	5145	4.077	80.1	0.31	−4.63	15 572
	CASPT2	4962	4.050	82.3	0.34	−1.97	15 710
	CCSD	4946	4.304	61.1	0.19		15 193
	[41][exp]						≈15 700
	[41]	5523	4.14	79			15 261
$4\,^2\Sigma^+$	MRCI	5260	4.283	95.2	0.43	−3.70	15 464
	CASPT2	5128	4.272	94.1	0.43	−1.81	15 550
	CCSD	4237	4.391	87.8	0.45		15 916
	[41][exp]						≈15 700
	[41]	5551	4.32	96			15 241

[exp]experimental results.

TABLE III. Parameters for the electronically excited states of RbSr, obtained with the MRCI, CASPT2, and CCSD approaches. Results from previous publications are also listed.

State	Ref.	D_e(cm^{-1})	r_e(Å)	ω_e(cm^{-1})	$\omega_e x_e$(cm^{-1})	μ_e(D) [102]	T_0(cm^{-1})
$X\,^2\Sigma^+$	MRCI	1298	4.564	42.5	0.35	1.70	
	CASPT2	1198	4.576	41.1	0.35	1.47	
	CCSD	778	4.787	33.6	0.36		
	[38]^{exp}			42 ± 5			
	[40]	1273	4.590	42.2			
	[55]	1041	4.667	38.1			
	[54]	1018	4.671	36.0			
	[44]	916	4.72	36		1.41	
	[53]	1073	4.599	32.3		1.54	
$1\,^2\Pi$	MRCI	8890	3.895	80.5	0.18	5.54	5164
	CASPT2	8621	3.887	81.0	0.19	5.42	5334
	CCSD	7687	3.946	79.6	0.21		5851
	[40]	8705	3.922	79.3			5094
	[55]	8440	3.868	79.5			
	[55]	8039	3.926	83.2			
$2\,^2\Sigma^+$	MRCI	5214	4.507	59.5	0.17	2.02	8830
	CASPT2	4948	4.519	58.6	0.17	0.12	8996
	CCSD	4340	4.554	58.4	0.20		9188
	[40]	5078	4.533	58.5			8711
	[55]	4983	4.445	58.4			
	[55]	4610	4.503	60.2			
$2\,^2\Pi$	MRCI	4556	4.111	66.5	0.24	9.61	11 457
	CASPT2	4194	4.105	66.4	0.26	8.63	11 719
	CCSD	2989	4.211	60.4	0.31		12 505
	[39]^{exp}						≈11 800
	[40]	4406	4.150	65.2			11 397
	[55]	4421	4.048	67.6			
	[55]	3304	4.170	63.4			
$3\,^2\Sigma^+$	MRCI	3791	4.143	59.2	0.23	7.13	12 218
	CASPT2	3565	4.150	51.4	0.19	6.50	12 341
	CCSD	2614	4.170	54.7	0.28		12 877
	[39]^{exp}						≈12 200
	[40]	3610	4.184	52.8			12 186
	[55]	3828	4.059	65.3			
	[55]	2892	4.133	62.5			
$1\,^4\Pi$	MRCI	3079	4.312	57.8	0.27	3.65	12 929
	CASPT2	2984	4.309	57.7	0.28	3.28	12 925
	CCSD	2568	4.358	54.9	0.29		12 923
	[40]	3036	4.333	56.9			12 762
	[55]	2838	4.265	57.0			
	[55]	2656	4.360	55.0			
$1\,^4\Sigma^+$	MRCI	391	6.148	16.5	0.17	−2.71	15 596
	CASPT2	394	6.141	16.3	0.17	−3.23	15 494
	CCSD	304	6.269	14.7	0.18		15 167
	[40]	390	6.171	16.2			15 387
	[55]	336	6.154	15.4			
	[55]	329	6.250	15.0			
$3\,^2\Pi$	MRCI	5391	4.338	57.2	0.15	−7.77	14 168
	CASPT2	5174	4.346	52.5	0.13	−5.57	14 283
	CCSD	5830	4.286	60.0	0.15		13 215
	[39]^{exp}						≈14 900
	[40]	5597	4.360	56.9			14 976
$4\,^2\Sigma^+$	MRCI	6185	4.511	78.4	0.25	−0.91	13 385
	CASPT2	6135	4.446	82.6	0.28	3.15	13 337
	CCSD	4130	4.544	75.1	0.34		14 922
	[39]^{exp}			86(3)			14 028(1)
	[40]	6282	4.510	78.0			14 301

^{exp}, experimental results.

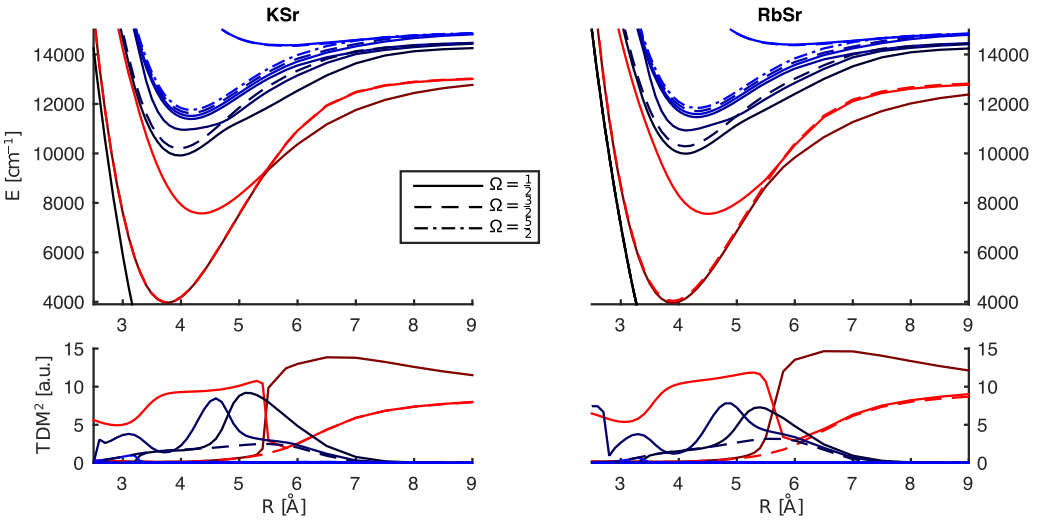

FIG. 5. Potential energy curves and transition dipole moments for KSr and RbSr including spin-orbit interaction.

Most prominent is an avoiding crossing which appears for the 2 $\Omega = 1/2$ and the 3 $\Omega = 1/2$ state between 5 and 6 Å. It shows a repulsion between the two states changing their angular momentum projection character from Σ^+ ($2\,^2\Sigma^+$) to Π ($1\,^2\Pi$) and *vice versa*. As a consequence, the formerly rather constant TDM of the $2\,^2\Sigma^+$ state [solid red (light gray) curve in the TDM subplots in Figs. 3 and 4] is replaced by two separate contributions in Fig. 5 [red (highest TDM line at small radii) and brown (highest line at large radii)] with a discontinuity in the range of the avoided crossing.

Several similar avoided crossings occur for the higher exited states. We extracted the parameters of the spin-orbit states and put them into the Supplemental Material which also includes figures for KCa and RbCa [76].

We note that the inclusion of spin-orbit coupling plays a big role in these regions since it changes the character of the corresponding wave functions significantly, which leads to abrupt changes in the dipole transition moment. Furthermore, it introduces strong deviations of the PES from typical shapes, making a numerical evaluation of the vibrational levels inevitable. The impact of SO correction on the vibrational states will be discussed in the next part.

IV. VIBRATIONAL ANALYSIS

In this section we focus on the vibrational analysis of the selected PES and discuss potential de-excitation mechanisms with the help of graphical illustrations of FC integrals.

A. Graphical representations of Franck-Condon overlap integrals

A convenient way of presenting the FC overlap integrals for a given electronic transition and a chosen ΔJ is a graphical matrix representation with element (i, j) referring to the overlap between the ith vibrational level of the ground state and the jth vibrational level of the excited state. The magnitude of each value is given as the z value and commonly represented by a color map. In the given context of finding suitable combinations of vibronic transitions for a coherent de-excitation such a representation is particularly useful, since potential "pathways" correspond to two large coefficients, one for a high vibrational level and one for the vibrational ground state of the electronic ground state, which belong to the same vibrational level of the corresponding electronically excited state.

Obviously, the overlap diagram for an idealized situation of having two exactly identical potential curves in the ground and excited state would correspond to a unit matrix. Given a situation of two shifted, but otherwise identical harmonic potentials, yields a Poisson distribution of intensities. How-

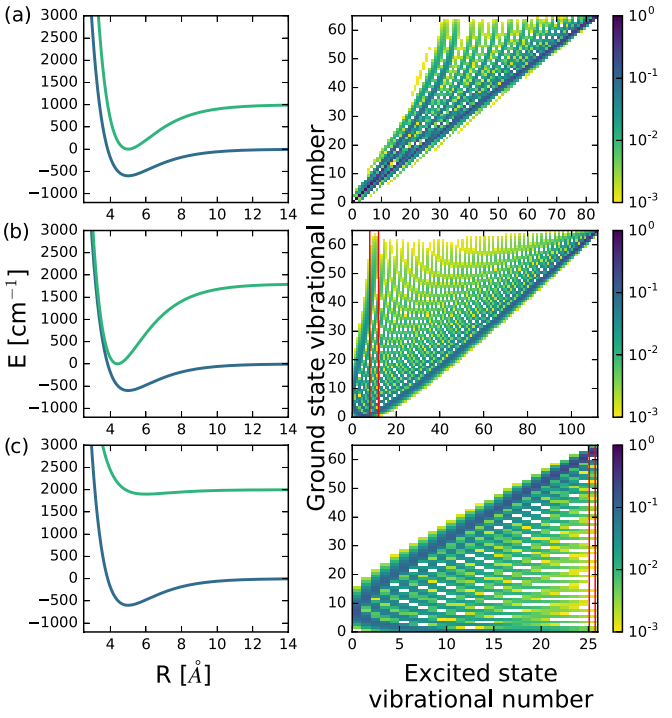

FIG. 6. Franck-Condon factors calculated from Morse potentials. Varying of the parameters for the excited state shows possible configurations for efficient transfer schemes.

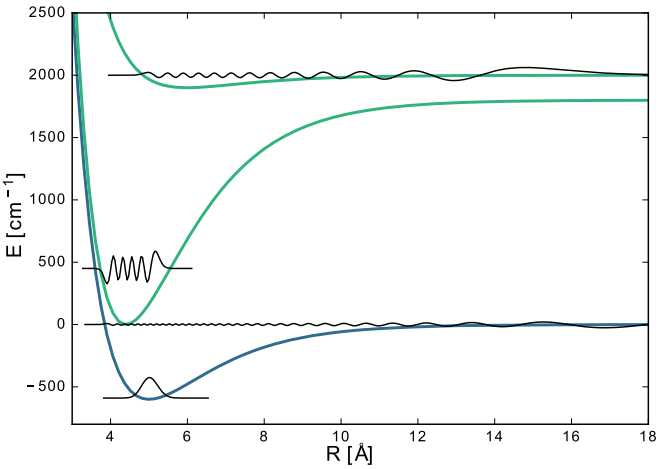

FIG. 7. Depiction of the nuclear wave functions involved in the transfer schemes for the cases of a tight bound excited state (case b) and a loosely bound excited state (case c).

ever, in cases of arbitrary potential curvatures and relative positioning an interpretation of the overlap graphics is less obvious. For this reason, and the added benefit of a better understanding of our actual results shown later, we start with a discussion of idealized cases.

A selection of stylized but typical scenarios is presented in Fig. 6. Our interpretation of the actual results for the *AK-AKE* systems under investigation will make use of these template graphics as a reference. The fictitious potential energy curves are based on Morse potentials [101] of the form,

$$V(r) = D_e(e^{-2\alpha(r-r_e)} - 2e^{-\alpha(r-r_e)}). \tag{7}$$

The parameters of the electronic ground-state potential are kept fixed at $D_e = 600$ cm^{-1}, $\alpha = 0.6$ Å^{-1}, and $r_e = 5.0$ Å, while the parameters for the excited state are varied to study the impact of shape variations and relative positioning on the FC factors. Figure 6(a) depicts the Franck-Condon overlap with a slightly deeper but otherwise identical Morse potential ($D_e = 1000$ cm^{-1}, $\alpha = 0.6$ Å^{-1}, and $r_e = 5.0$ Å) as excited state. Due to the unchanged equilibrium distance the main branch starts off diagonally from the (0,0) corner. The deeper potential curve results in a larger number of vibrational states in the excited state and, in turn, changes the slope of the linear branch. Several secondary branches emerge from the main branch fanning out towards higher vibrational numbers in the ground state. However, no effective de-excitation pathway emerges in this situation. Figure 6(b) documents the case of a tightly bound excited state ($D_e = 1800$ cm^{-1}, $\alpha = 0.6$ Å^{-1}, and $r_e = 4.4$ Å). Here the Franck-Condon graphics show a fin-shaped structure with two main branches spreading out

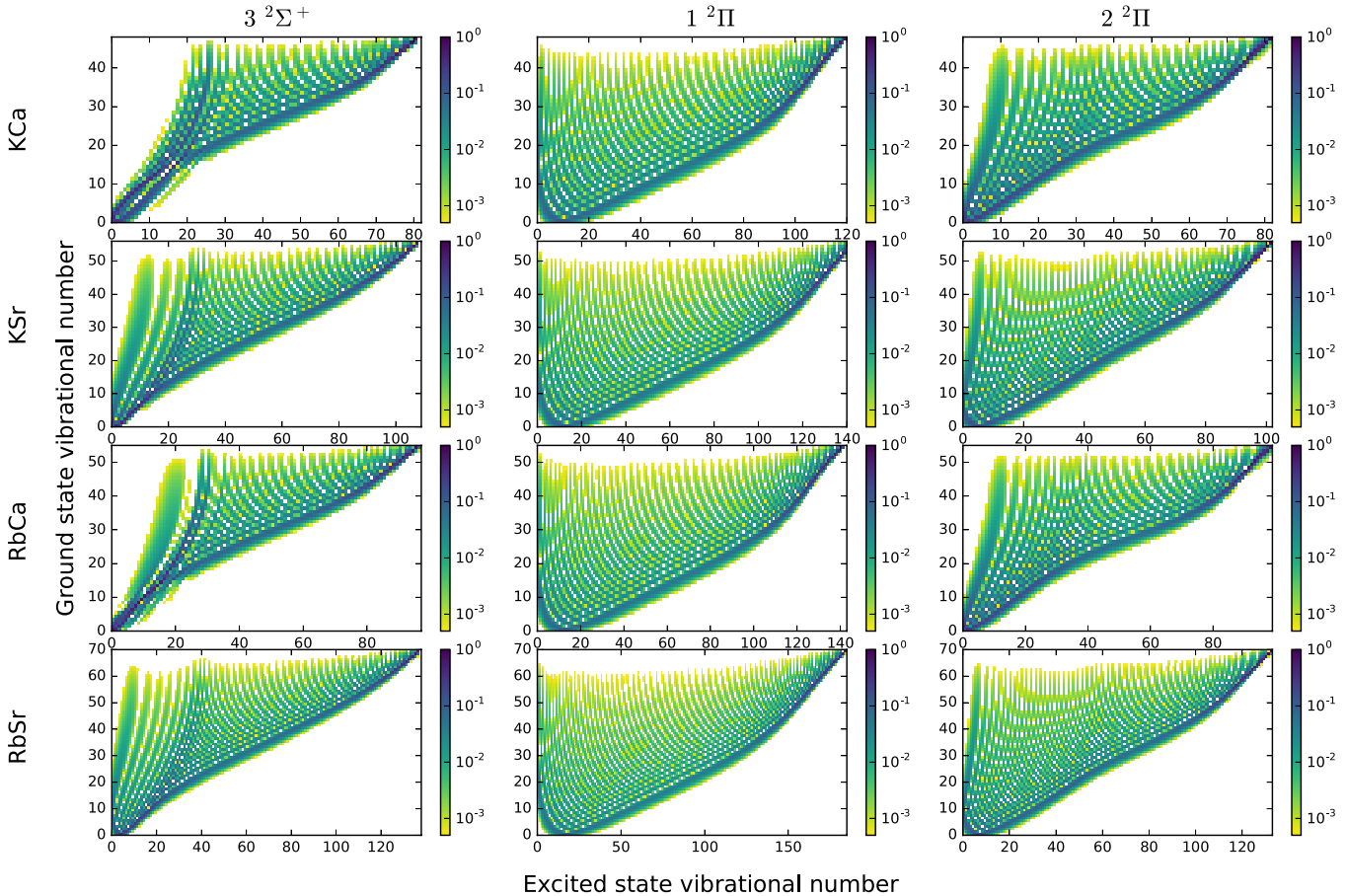

FIG. 8. Franck-Condon factors as a function of the ground-state vibrational number v'' and the excited state vibrational number v' for all four molecules (rows) and the three most relevant excited states $3^2\Sigma^+$, $1^2\Pi$, and $2^2\Pi$ in the doublet manifold (columns).

from a turning point on the axis of the excited state vibrational number, creating the impression of a reflection on the x axis. One branch exhibits linear behavior towards higher vibrational numbers in the excited state, where the slope is dependent on the difference of the potential depths D_e and potential widths α. The other branch features a parabolic form at small vibrational numbers until it is "reflected" again at the y axis. Due to this feature there is a large overlap of the nuclear wave function $|\nu' = 10\rangle$ with both the highest vibrational state and the vibrational ground state of the electronic ground state. This feature opens potential pathways for a coherent de-excitation. The corresponding vibrational wave functions are shown in Fig. 7. In Fig. 6(c) a loosely bound excited state with large equilibrium distance is used ($D_e = 100$, $\alpha = 0.6$, and $r_e = 6.0$ Å). The resulting Franck-Condon matrix shows similar behavior as Fig. 6(b), but is mirrored along the image diagonal. In this case, the highest vibrational state in the excited state exhibits large overlap with both the highest vibrational state and the vibrational ground state of the electronic ground state. The vibrational wave functions for this desirable situation are sketched in Fig. 7.

B. Vibrational analysis of the doublet states

Figure 8 contains the FC graphics for vibrational transitions between the ground state and the three most relevant excited states ($3^2\Sigma^+$, $1^2\Pi$, and $2^2\Pi$) for the MRCI potential curves. In general, differences in potential depth, width, position, and reduced mass lead to an increase in the number of vibrational levels when going from Li-M_{AKE} to Rb-M_{AKE}. The $2^2\Sigma^+$ state has been skipped since it is very similar in shape to Fig. 6(a) with an equilibrium distance close to the ground-state value, which leads to rather diagonal Franck-Condon matrices and therefore inefficient de-excitation pathways.

The $3^2\Sigma^+$ state, on the other hand, shows an unusual functional course due to an avoided crossing with the $4^2\Sigma^+$ state. The main branch of the $3^2\Sigma^+$ state Franck-Condon factors runs nearly linear with a slope of about 0.5, starting off with a slightly negative curvature and switches to a strictly linear behavior again after a small kink at about 65%–75% of the maximum vibrational number ν'_{max}. Secondary branches extend from the (0,0) corner towards high ground-state vibrational numbers at relatively low excited state vibrational numbers. For LiSr (see Supplemental Material [76]), only a few secondary branches emerge, while more secondary branches appear for the heavier molecules. These branches can be used as an efficient transfer path from a high vibronic state in the ground state to the excited state.

The FC graphics for the two $^2\Pi$ states look very similar to each other due to their similar equilibrium bond distances. Both are most closely resembling case (b) of our template selection, and are therefore good candidates for coherent de-excitation. They feature a similar reflection of the main branch on the x axis (corresponding to the excited state vibrational number), which stems from the shorter equilibrium distance in comparison to the ground state. The turning point for the $1^2\Pi$ state lies at higher vibrational numbers because of the smaller bond distance. After reflection on the x axis the main branch shows linear behavior with a slope of about $1/3$ and $1/2$ for the $1^2\Pi$ and the $2^2\Pi$, respectively. At about 65%–75% of the highest vibrational number ν'_{max} the linear function shows a kink and switches to a steeper slope due to the changes in the PES character at long range.

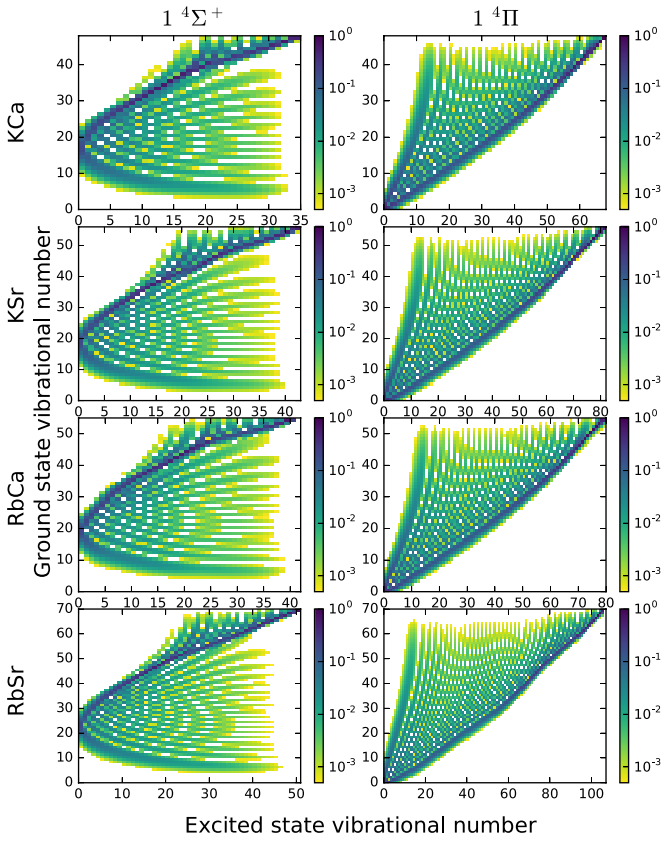

FIG. 9. Franck-Condon factors as a function of the ground-state vibrational number ν'' and the excited state vibrational number ν' for all four molecules (rows) and two excited states ($1^4\Sigma^+$ and $1^4\Pi$) in the quartet manifold (columns).

C. Vibrational analysis of the quartet states

For the sake of an extended comparison we also investigated the $1^4\Sigma^+$ and the $1^4\Pi$ states of the quartet manifold despite the vanishing transition dipole moment for excitations from the $X^2\Sigma^+$ ground state. The corresponding Franck-Condon graphics are depicted in Fig. 9. The $1^4\Pi$ state and the ground state have a similar equilibrium distance. Therefore, the FC graphics show a largely diagonal structure with secondary branches towards higher vibrational numbers in the ground state. Since an antibonding orbital is occupied in the $1^4\Sigma^+$ state the potential curve is shallow (on the order of a few hundred cm^{-1}) and shows a large equilibrium distance. This leads to a turning point on the ground-state axis of the Franck-Condon matrices, and the graphics are most closely resembling case (c) of our template selection. In principle, this structure can also provide efficient transfer schemes, as has been shown in Sec. IV A. The position of the turning point, and consequently, the efficiency of the de-excitation, are strongly dependent on the equilibrium distance. Out of the investigated molecules only LiSr shows significant Franck-Condon factors for this alternative de-excitation mechanism, see Supplemental Material [76].

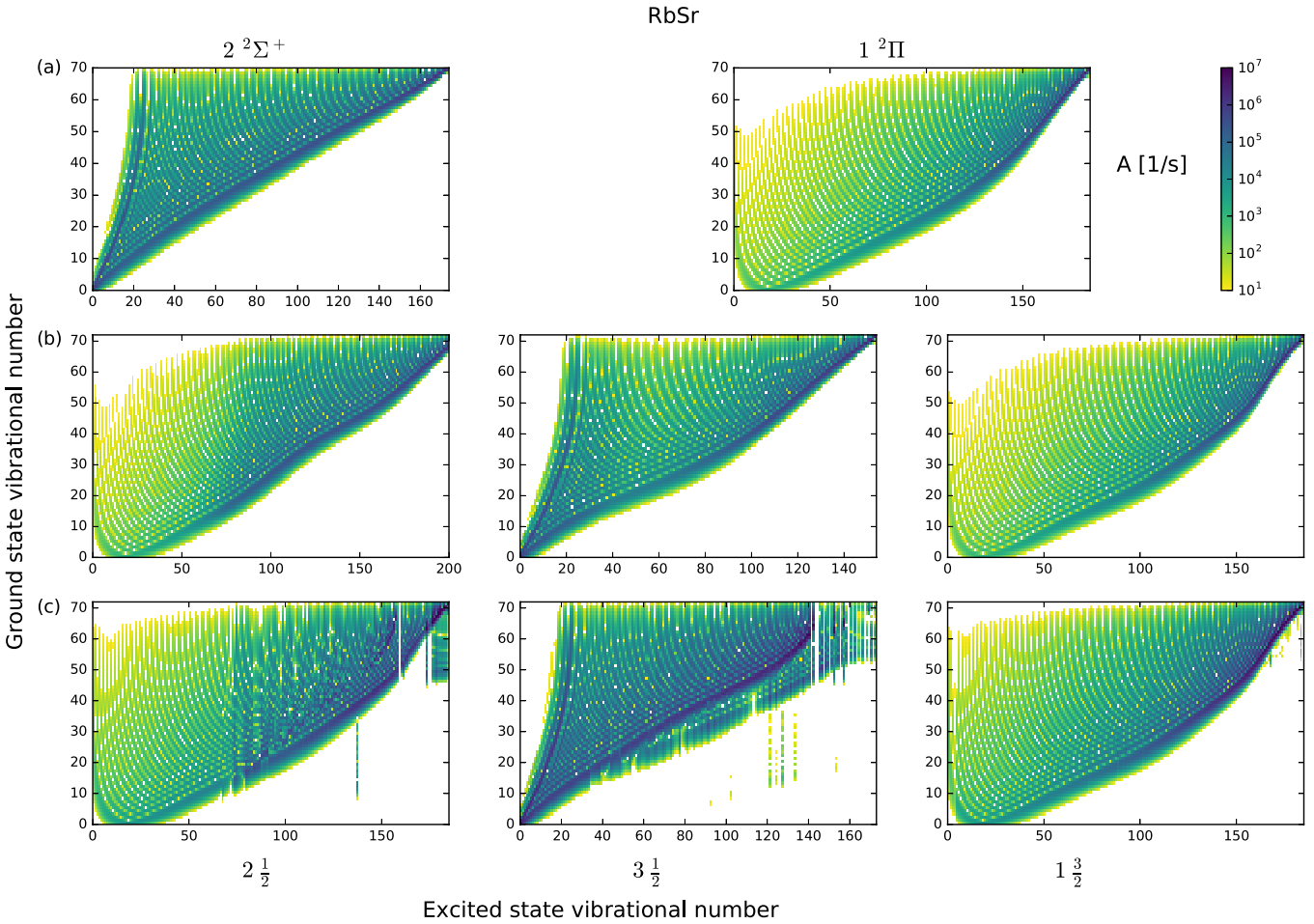

FIG. 10. Comparison of Einstein *A* coefficient graphics obtained with different strategies for the inclusion spin-orbit coupling. (a) In Hund's case (a) the spin-orbit coupling is completely neglected. (b) Spin-orbit coupling is introduced via effective matrix elements as described in Sec. II B. (c) For intermediate coupling we used the DUO program and included spin-orbit coupling effects via the distance-dependent spin-orbit matrix elements obtained from *ab initio* calculations.

D. Impact of spin-orbit coupling on the vibrational analysis

For the heavier diatomics spin-orbit coupling effects become non-negligible and have to be taken into consideration in the rovibrational analysis. This is done either via the method described in Sec. II B or via the DUO program package [75]. In the latter case, the distance dependent spin-orbit coupling matrix elements, determined by extended MRCI calculations in MOLPRO, are used to couple rovibronic states. After the coupling, Λ and Σ are no longer good the quantum numbers, but an approximate assignment is still possible. However, this leads to discontinuities in the matrix elements of Fig. 10(c), which shows the effect of the spin-orbit coupling on the Einstein *A* coefficients. In the case of the lower asymptote two $\Omega = \frac{1}{2}$ and one $\Omega = \frac{3}{2}$ states arise. If spin-orbit interaction is taken into account by the effective Hamiltonian the first two can interact and show an avoided crossings; see Fig. 5. The 2 $\Omega = \frac{1}{2}$ state corresponds at short ranges to 1 $^2\Pi$ and at long ranges to 2 $^2\Sigma^+$. This leads to related similarities for low (1 $^2\Pi$) or high (2 $^2\Sigma^+$) vibrational quantum numbers as can be seen in Fig. 10(b). The situation is reversed for the 3 $\Omega = \frac{1}{2}$ state. In the DUO package the spin-orbit coupling is included as coupling between prior calculated Hund's case (a) rovibronic states. Therefore, two edges can now be observed for the 3 $\Omega = \frac{1}{2}$ state corresponding to the two different MRCI potentials. The 2 $\Omega = \frac{1}{2}$ show instead a loss of structure for the Einstein *A* coefficients in this region. The 1 $\Omega = \frac{3}{2}$ is not influenced by the spin-orbit coupling and corresponds to the 1 $^2\Pi$ state. For the influence on the transition energies we refer the interested reader to the Supplemental Material [76], where we also discuss the effect of the spin-orbit coupling on the less accessible states of the ^3P asymptote.

E. Transition probabilities

For experimentalists, the most relevant information is contained in the Einstein *A* coefficients of the selected vibronic transitions. Here, a slightly different graphical representation shown in Fig. 11 is useful, where the magnitudes of the Einstein *A* coefficients are plotted as a function of the transition energies. The figure contains those Einstein *A* coefficients which are relevant for a transfer from the highest to the lowest vibrational level of the ground state via an arbitrary vibrational level of the selected electronically excited state. For a simplified interpretation we shifted the transition energies by the energy difference between the highest and the lowest vibrational level of each ground state. This way, the two

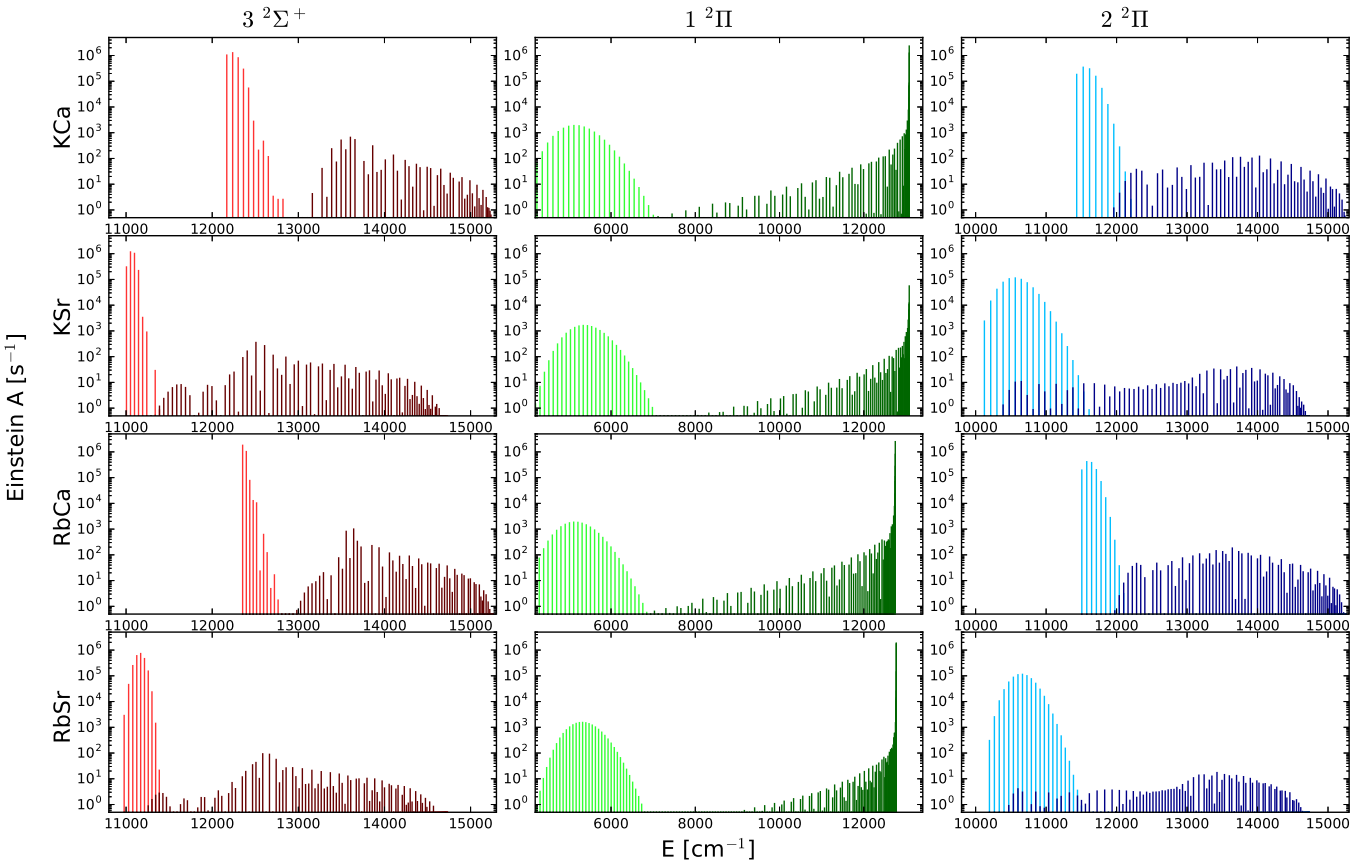

FIG. 11. Einstein A coefficients for the three most relevant excited states $3^2\Sigma^+$, $1^2\Pi$, and $2^2\Pi$ in the doublet manifold. Darker colors are used for the Einstein A coefficients of transitions from the highest vibrational level of the ground state to an arbitrary vibrational level of the denoted excited state. The corresponding transition energies can be read from the x axis. Brighter colors are used for the Einstein A coefficients of transitions between an arbitrary vibrational level of the excited state into the lowest vibrational level of the ground states. To simplify the interpretation, we shifted their positions by the energy difference between the highest and lowest vibrational state of the ground state (see text).

relevant lines for the same vibrational level (excitation and de-excitation) lie at the same position. The shift values are 1437.7, 1356.8, 1321.4, and 1279.3 cm^{-1} for KCa, KSr, RbCa, and RbSr, respectively. In this way, it is obvious that a combination of excitation and de-excitation transitions is suitable only for overlapping features in the figure.

For the $2\,^2\Sigma^+$ state, no vibrational level can provide Einstein A factors larger than 1 s^{-1} for the proposed two-step transfer mechanism. Therefore, this state has been skipped again in the detailed analysis. The most promising candidate for this mechanism is the $2\,^2\Pi$ state, especially for RbSr and KSr. For these molecules, there are several states in the region from 10 500 to 11 500 cm^{-1} with Einstein A factors of about 10 s^{-1} for electronic excitation from the highest vibrational level and of about 10^4 s^{-1} for a de-excitation into the lowest vibrational state of the electronic ground state. Regarding the first step of the proposed mechanism, we only find Einstein A coefficients larger than 10^4 s^{-1} for excitations into high vibrational levels of the $2\,^2\Sigma^+$ or $1\,^2\Pi$ state, with energies that are at most 100 cm^{-1} below the ^2P asymptote of the corresponding AK atom. The Einstein A coefficients for the excitation can be increased by about one order of magnitude if the second highest vibrational level ($v_{max} - 1$) of the electronic ground state is used as a starting point instead of the highest one. This vibrational state is better localized and overlaps better with the vibrational levels of the excited state. The behavior of the Einstein A coefficients for this state ($v_{max} - 1$) is similar to the dark ones shown in Fig. 11 with an increased magnitude.

In a recent publication the STIRAP scheme has been reviewed and a formula for the calculation of laser intensities using Einstein A factors was presented [95]. According to this, Einstein A coefficients larger than 10^4 s^{-1} are desirable for the individual transitions, which is not fulfilled for the first step of the proposed mechanism (see Fig. 11). For example, in the case of the $2\,^2\Pi$ state of KSr or RbSr, the first step only yields $A = 10\ s^{-1}$, while the second step has a significantly higher A value between 10^4 and 10^5 s^{-1}. Nevertheless, transfer probabilities might be enhanced by Feshbach resonances [103–105] or accidental resonances between rovibronic states [106].

Note that the results presented in Fig. 11 do not include spin-orbit coupling. For brevity, a discussion of spin-orbit effects on the Einstein A coefficients has been shifted to the Supplemental Material [76].

V. CONCLUSION

We calculated the PES for the first few electronically excited states with asymptotes corresponding to s-p excitations on the

AK or the *AKE* atom. A comparison with experimental data, which is only available for a small selection of states and molecules (LiCa, RbCa, and RbSr), indicates that MRCI and CASPT2 approaches are better suited for the prediction of line positions than CCSD and EOM-CCSD if triplet corrections are neglected. Furthermore, the inclusion of spin-orbit coupling is necessary to obtain more realistic PES curvatures and to improve the description of the transition dipole moment dependency on the internuclear distance.

Regarding the shape of the PES, equilibrium distances of the various doublet states of one molecule do not differ by more than about 0.6 Å. Typically, the dissociation energies in the excited states exceed the weakly bound ground states by a factor of three at least. In general, the Π states are more strongly bound and show a tendency to slightly shorter equilibrium bond lengths in all molecules. The potential shape of the $3^2\Sigma^+$ and $4^2\Sigma^+$ states is strongly influenced by an avoided crossing between the two states close to the equilibrium position which also results in a change of the transition dipole moment. By including spin-orbit coupling changes due to avoided crossings appear for several states, for example, for the former $2^2\Sigma^+$ state.

The PES analysis was followed by a study of transition dipole moments for the selected states. Particularly interesting in the context of coherent de-excitation are the $2^2\Sigma^+$, $3^2\Sigma^+$, $1^2\Pi$, and $2^2\Pi$ excited states with vibrational bands within the range of Ti:sapphire laser systems. For the $^2\Sigma^+$ and the $^2\Pi$ states corresponding to the ^2P(AK) asymptote we found considerable transition dipole moments for large internuclear separations which remained fairly constant for the $^2\Sigma^+$ state over a wide range of distances. The transition dipole moments for other states are comparably small except for the $3^2\Sigma^+$ states of K-M_{AKE} and Rb-M_{AKE}, which show a peak at typical bond distances. Additionally, the transition dipole moments of the $3^2\Sigma^+$ and $4^2\Sigma^+$ states are modulated due to an avoided crossing between them.

Finally, we performed a vibrational analysis of the first few electronically excited states. In general, the $2\ ^2\Sigma^+$ state does not provide sufficiently large Einstein *A* factors for a two-step transfer from a vibrationally highly excited level of the electronic ground state to the lowest vibrational level of the electronic ground state. A much more promising candidate for this mechanism is the $2\ ^2\Pi$ state, in particular for RbSr and KSr, where several states in the region from 10500 to 11500 cm^{-1} show sufficiently large Einstein *A* factors. Regarding only the first step of the proposed mechanism, both the $2\ ^2\Sigma^+$ and $1\ ^2\Pi$ state of the heavy *AK*-*AKE* molecules show very large Einstein *A* factors close to the ^2P asymptote of the *AK* atom, which could be the starting point for more sophisticated de-excitation mechanisms involving several excited states.

ACKNOWLEDGMENTS

The authors thank Florian Schreck for stimulating discussions on the subject. The authors gratefully acknowledge support from NAWI Graz. This research was supported by the Austrian Science Fund (FWF) under Grant No. 22962-N20 as well as the European Commission and the Styrian Government within the ERDF program.

[1] J. Ulmanis, J. Deiglmayr, M. Repp, R. Wester, and M. Weidemuller, Chem. Rev. **112**, 4890 (2012).
[2] G. Quéméner and P. S. Julienne, Chem. Rev. **112**, 4949 (2012).
[3] I. Bloch and P. Zoller, in *Ultracold Bosonic and Fermionic Gases*, edited by A. L. F. Kathryn Levin and D. M. Stamper-Kurn, Contemporary Concepts of Condensed Matter Science, Vol. 5 (Elsevier, Amsterdam, 2012), pp. 121–156.
[4] L. D. Carr, D. DeMille, R. V. Krems, and J. Ye, New J. Phys. **11**, 055049 (2009).
[5] J. Doyle, B. Friedrich, R. Krems, and F. Masnou-Seeuws, Eur. Phys. J. D **31**, 149 (2004).
[6] M. Baranov, L. Dobrek, K. Goral, L. Santos, and M. Lewenstein, Phys. Scr. **T102**, 74 (2002).
[7] L. Santos, G. V. Shlyapnikov, P. Zoller, and M. Lewenstein, Phys. Rev. Lett. **85**, 1791 (2000).
[8] K. Goral, L. Santos, and M. Lewenstein, Phys. Rev. Lett. **88**, 170406 (2002).
[9] L. D. Carr, G. V. Shlyapnikov, and Y. Castin, Phys. Rev. Lett. **92**, 150404 (2004).
[10] M. A. Baranov, L. Dobrek, and M. Lewenstein, Phys. Rev. Lett. **92**, 250403 (2004).
[11] H. P. Buchler, E. Demler, M. Lukin, A. Micheli, N. Prokof'ev, G. Pupillo, and P. Zoller, Phys. Rev. Lett. **98**, 060404 (2007).
[12] M. A. Baranov, M. Dalmonte, G. Pupillo, and P. Zoller, Chem. Rev. **112**, 5012 (2012).
[13] D. DeMille, Phys. Rev. Lett. **88**, 067901 (2002).
[14] B. K. Stuhl, M. T. Hummon, and J. Ye, Annu. Rev. Phys. Chem. **65**, 501 (2014).
[15] R. V. Krems, Phys. Chem. Chem. Phys. **10**, 4079 (2008).
[16] E. R. Hudson, C. Ticknor, B. C. Sawyer, C. A. Taatjes, H. J. Lewandowski, J. R. Bochinski, J. L. Bohn, and J. Ye, Phys. Rev. A **73**, 063404 (2006).
[17] C. Chin, V. V. Flambaum, and M. G. Kozlov, New J. Phys. **11**, 055048 (2009).
[18] M. Kajita, G. Gopakumar, M. Abe, and M. Hada, J. Phys. B **46**, 025001 (2013).
[19] M. Kajita, G. Gopakumar, M. Abe, and M. Hada, J. Mol. Spectrosc. **300**, 99 (2014).
[20] V. V. Flambaum and M. G. Kozlov, Phys. Rev. Lett. **99**, 150801 (2007).
[21] E. R. Meyer and J. L. Bohn, Phys. Rev. A **80**, 042508 (2009).
[22] E. R. Meyer, J. L. Bohn, and M. P. Deskevich, Phys. Rev. A **73**, 062108 (2006).
[23] K. Beloy, A. W. Hauser, A. Borschevsky, V. V. Flambaum, and P. Schwerdtfeger, Phys. Rev. A **84**, 062114 (2011).
[24] E. R. Hudson, H. J. Lewandowski, B. C. Sawyer, and J. Ye, Phys. Rev. Lett. **96**, 143004 (2006).
[25] J. F. Barry, D. J. McCarron, E. B. Norrgard, M. H. Steinecker, and D. DeMille, Nature (London) **512**, 286 (2014).
[26] J. M. Doyle, J. D. Weinstein, R. deCarvalho, T. Guillet, and B. Friedrich, Nature (London) **395**, 148 (1998).

[27] H. L. Bethlem, G. Berden, F. M. H. Crompvoets, R. T. Jongma, A. J. A. van Roij, and G. Meijer, Nature (London) **406**, 491 (2000).

[28] Y. B. Band and P. S. Julienne, Phys. Rev. A **51**, R4317(R) (1995).

[29] A. Fioretti, D. Comparat, A. Crubellier, O. Dulieu, F. Masnou-Seeuws, and P. Pillet, Phys. Rev. Lett. **80**, 4402 (1998).

[30] A. J. Leggett, Rev. Mod. Phys. **73**, 307 (2001).

[31] S. Stellmer, M. K. Tey, B. Huang, R. Grimm, and F. Schreck, Phys. Rev. Lett. **103**, 200401 (2009).

[32] P. S. Zuchowski, J. Aldegunde, and J. M. Hutson, Phys. Rev. Lett. **105**, 153201 (2010).

[33] B. Pasquiou, A. Bayerle, S. M. Tzanova, S. Stellmer, J. Szczepkowski, M. Parigger, R. Grimm, and F. Schreck, Phys. Rev. A **88**, 023601 (2013).

[34] T. Aoki, Y. Yamanaka, M. Takeuchi, Y. Torii, and Y. Sakemi, Phys. Rev. A **87**, 063426 (2013).

[35] C. Callegari and W. E. Ernst, in *Handbook of High-Resolution Spectroscopy*, edited by M. Quack and F. Merkt (John Wiley & Sons, Chichester, 2011), pp. 1551–1594.

[36] J. P. Toennies and A. F. Vilesov, Angew. Chem. Int. Edit. **43**, 2622 (2004).

[37] G. Krois, J. V. Pototschnig, F. Lackner, and W. E. Ernst, J. Phys. Chem. A **117**, 13719 (2013).

[38] F. Lackner, G. Krois, T. Buchsteiner, J. V. Pototschnig, and W. E. Ernst, Phys. Rev. Lett. **113**, 153001 (2014).

[39] G. Krois, F. Lackner, J. V. Pototschnig, T. Buchsteiner, and W. Ernst, Phys. Chem. Chem. Phys. **16**, 22373 (2014).

[40] J. V. Pototschnig, G. Krois, F. Lackner, and W. E. Ernst, J. Chem. Phys. **141**, 234309 (2014).

[41] J. V. Pototschnig, G. Krois, F. Lackner, and W. E. Ernst, J. Mol. Spectrosc. **310**, 126 (2015).

[42] J. V. Pototschnig, A. W. Hauser, and W. E. Ernst, Phys. Chem. Chem. Phys. **18**, 5964 (2016).

[43] J. Deiglmayr, M. Aymar, R. Wester, M. Weidemueller, and O. Dulieu, J. Chem. Phys. **129**, 064309 (2008).

[44] G. Gopakumar, M. Abe, M. Hada, and M. Kajita, J. Chem. Phys. **140**, 224303 (2014).

[45] A. Micheli, G. K. Brennen, and P. Zoller, Nat. Phys. **2**, 341 (2006).

[46] L. M. Russon, G. K. Rothschopf, M. D. Morse, A. I. Boldyrev, and J. Simons, J. Chem. Phys. **109**, 6655 (1998).

[47] A. Stein, M. Ivanova, A. Pashov, H. Knöckel, and E. Tiemann, J. Chem. Phys. **138**, 114306 (2013).

[48] A. R. Allouche and M. Aubert-Frécon, Chem. Phys. Lett. **222**, 524 (1994).

[49] S. Kotochigova, A. Petrov, M. Linnik, J. Klos, and P. S. Julienne, J. Chem. Phys. **135**, 164108 (2011).

[50] G. Gopakumar, M. Abe, M. Kajita, and M. Hada, Phys. Rev. A **84**, 062514 (2011).

[51] G. Gopakumar, M. Abe, M. Hada, and M. Kajita, Phys. Rev. A **84**, 045401 (2011).

[52] G. Gopakumar, M. Abe, M. Hada, and M. Kajita, J. Chem. Phys. **138**, 194307 (2013).

[53] R. Guerout, M. Aymar, and O. Dulieu, Phys. Rev. A **82**, 042508 (2010).

[54] T. Chen, S. B. Zhu, X. L. Li, J. Qian, and Y. Z. Wang, Phys. Rev. A **89**, 063402 (2014).

[55] P. S. Zuchowski, R. Guerout, and O. Dulieu, Phys. Rev. A **90**, 012507 (2014).

[56] P. J. Knowles and H.-J. Werner, Chem. Phys. Lett. **115**, 259 (1985).

[57] H.-J. Werner and P. J. Knowles, J. Chem. Phys. **82**, 5053 (1985).

[58] H.-J. Werner and P. J. Knowles, J. Chem. Phys. **89**, 5803 (1988).

[59] P. J. Knowles and H.-J. Werner, Theor. Chem. Acc. **84**, 95 (1992).

[60] H. J. Werner, Mol. Phys. **89**, 645 (1996).

[61] J. F. Stanton and R. J. Bartlett, J. Chem. Phys. **98**, 7029 (1993).

[62] W. Müller, J. Flesh, and W. Meyer, J. Chem. Phys. **80**, 3297 (1984).

[63] W. Müller and W. Meyer, J. Chem. Phys. **80**, 3311 (1984).

[64] B. P. Prascher, D. E. Woon, K. A. Peterson, T. H. Dunning, and A. K. Wilson, Theor. Chem. Acc. **128**, 69 (2011).

[65] I. S. Lim, P. Schwerdtfeger, B. Metz, and H. Stoll, J. Chem. Phys. **122**, 104103 (2005).

[66] I. S. Lim, H. Stoll, and P. Schwerdtfeger, J. Chem. Phys. **124**, 034107 (2006).

[67] In the case of K and Ca the 10 innermost electrons were replaced by the effective core potential ECP10MDF, for Rb and Sr we replaced the 28 electrons by the effective core potential ECP28MDF.

[68] The basis sets were used in decontracted form and have been extended by the following additional basis functions: K[s: 0.0037, 0.0017; p: 0.0016, 0.00062; d: 4.34, 0.011; f: 0.0296]; Rb[s: 0.0036, p: 0.0042, d: 0.0116, 2.860, f: 0.0624 g: 0.33] .

[69] H. D. Li, H. Feng, W. G. Sun, Y. Zhang, Q. C. Fan, K. A. Peterson, Y. M. Xie, and H. F. Schaefer, Mol. Phys. **111**, 2292 (2013).

[70] The current version of CFOUR does not support the use of core polarization functions.

[71] Y. Ralchenko, A. Kramida, J. Reader, and NIST ASD Team, National Institute of Standards and Technology, Gaithersburg, MD, http://physics.nist.gov/asd (2015).

[72] We used the values $A_K = 19.24\,\mathrm{cm}^{-1}$, $A_{Rb} = 79.2\,\mathrm{cm}^{-1}$, $A_{Ca} = 52.7\,\mathrm{cm}^{-1}$, and $A_{Sr} = 193.7\,\mathrm{cm}^{-1}$ for K, Rb, Ca, and Sr, respectively. For the remaining atoms the spin-orbit splitting effects are small, with constants $A_{\mathrm{Li}} = 0.1\,\mathrm{cm}^{-1}$ and $A_{\mathrm{Na}} = 5.7\,\mathrm{cm}^{-1}$.

[73] M. Tomza, F. Pawlowski, M. Jeziorska, C. P. Koch, and R. Moszynski, Phys. Chem. Chem. Phys. **13**, 18893 (2011).

[74] H.-J. Werner, P. J. Knowles, G. Knizia, F. R. Manby, M. Schütz, P. Celani, T. Korona, R. Lindh, A. Mitrushenkov, G. Rauhut, K. R. Shamasundar, T. B. Adler, R. D. Amos, A. Bernhardsson, A. Berning, D. L. Cooper, M. J. O. Deegan, A. J. Dobbyn, F. Eckert, E. Goll, C. Hampel, A. Hesselmann, G. Hetzer, T. Hrenar, G. Jansen, C. Köppl, Y. Liu, A. W. Lloyd, R. A. Mata, A. J. May, S. J. McNicholas, W. Meyer, M. E. Mura, A. Nicklass, D. P. O'Neill, P. Palmieri, D. Peng, K. Pflüger, R. Pitzer, M. Reiher, T. Shiozaki, H. Stoll, A. J. Stone, R. Tarroni, T. Thorsteinsson, and M. Wang, Computer code MOLPRO, Version 2012.1, a package of *ab initio* programs, 2012, http://www.molpro.net.

[75] S. N. Yurchenko, L. Lodi, J. Tennyson, and A. V. Stolyarov, Comput. Phys. Commun. **202**, 262 (2016).

[76] See Supplemental Material at http://link.aps.org/supplemental/10.1103/PhysRevA.95.022501 for additional tables and figures comparing different *ab initio* methods and tables listing the spectroscopic parameters of the spin-orbit states.

[77] P. J. Knowles and H.-J. Werner, Chem. Phys. Lett. **145**, 514 (1988).

[78] P. Celani and H. J. Werner, J. Chem. Phys. **112**, 5546 (2000).

[79] J. Stanton, J. Gauss, M. Harding, and P. Szalay, CFOUR, coupled-cluster techniques for computational chemistry, a quantum-chemical program package, with contributions from A. A. Auer, R. J. Bartlett, U. Benedikt, C. Berger, D. E. Bernholdt, Y. J. Bomble, L. Cheng, O. Christiansen, M. Heckert, O. Heun, C. Huber, T.-C. Jagau, D. Jonsson, J. Jusélius, K. Klein, W. J. Lauderdale, F. Lipparini, D. A. Matthews, T. Metzroth, L. A. Mück, D. P. O'Neill, D. R. Price, E. Prochnow, C. Puzzarini, K. Ruud, F. Schiffmann, W. Schwalbach, C. Simmons, S. Stopkowicz, A. Tajti, J. Vázquez, F. Wang, J. D. Watts and the integral packages MOLECULE (J. Almlöf and P. R. Taylor), PROPS (P. R. Taylor), ABACUS (T. Helgaker, H. J. Aa. Jensen, P. Jørgensen, and J. Olsen), and ECP routines by A. V. Mitin and C. van Wüllen.

[80] R. J. Le Roy, *betaFit 2.1*, a Computer Program to Fit Pointwise Potentials to Selected Analytic Functions, University of Waterloo Chemical Physics Research Report CP-666 (University of Waterloo, Waterloo, 2013).

[81] J. Jiang, Y. J. Cheng, and J. Mitroy, J. Phys. B: At. Mol. Opt. Phys. **46**, 125004 (2013).

[82] R. J. LeRoy, *University of Waterloo Chemical Physics Research Report CP-663* (University of Waterloo, Waterloo, 2007), http://leroy.uwaterloo.ca/programs/.

[83] J. Deiglmayr, A. Grochola, M. Repp, K. Mortlbauer, C. Gluck, J. Lange, O. Dulieu, R. Wester, and M. Weidemuller, Phys. Rev. Lett. **101**, 133004 (2008).

[84] A. J. Kerman, J. M. Sage, S. Sainis, T. Bergeman, and D. DeMille, Phys. Rev. Lett. **92**, 033004 (2004).

[85] C. Haimberger, J. Kleinert, M. Bhattacharya, and N. P. Bigelow, Phys. Rev. A **70**, 021402 (2004).

[86] A. Wakim, P. Zabawa, and N. P. Bigelow, Phys. Chem. Chem. Phys. **13**, 18887 (2011).

[87] J. T. Kim, Y. Lee, B. Kim, D. J. Wang, W. C. Stwalley, P. L. Gould, and E. E. Eyler, Phys. Rev. A **84**, 062511 (2011).

[88] J. T. Kim, Y. Lee, B. Kim, D. Wang, W. C. Stwalley, P. L. Gould, and E. E. Eyler, Phys. Chem. Chem. Phys. **13**, 18755 (2011).

[89] D. Wang, J. Qi, M. F. Stone, O. Nikolayeva, B. Hattaway, S. D. Gensemer, H. Wang, W. T. Zemke, P. L. Gould, E. E. Eyler, and W. C. Stwalley, Eur. Phys. J. D **31**, 165 (2004).

[90] K. Aikawa, D. Akamatsu, M. Hayashi, K. Oasa, J. Kobayashi, P. Naidon, T. Kishimoto, M. Ueda, and S. Inouye, Phys. Rev. Lett. **105**, 203001 (2010).

[91] N. Nemitz, F. Baumer, F. Münchow, S. Tassy, and A. Görlitz, Phys. Rev. A **79**, 061403(R) (2009).

[92] S. Dutta, J. Lorenz, A. Altaf, D. S. Elliott, and Y. P. Chen, Phys. Rev. A **89**, 020702 (2014).

[93] A. Altaf, S. Dutta, J. Lorenz, J. Perez-Rios, Y. P. Chen, and D. S. Elliott, J. Chem. Phys. **142**, 114310 (2015).

[94] A. Ridinger, S. Chaudhuri, T. Salez, D. R. Fernandes, N. Bouloufa, O. Dulieu, C. Salomon, and F. Chevy, EPL **96**, 33001 (2011).

[95] K. Bergmann, N. V. Vitanov, and B. W. Shore, J. Chem. Phys. **142**, 170901 (2015).

[96] F. Lang, K. Winkler, C. Strauss, R. Grimm, and J. Hecker Denschlag, Phys. Rev. Lett. **101**, 133005 (2008).

[97] K. K. Ni, S. Ospelkaus, M. H. G. de Miranda, A. Pe'er, B. Neyenhuis, J. J. Zirbel, S. Kotochigova, P. S. Julienne, D. S. Jin, and J. Ye, Science **322**, 231 (2008).

[98] S. Ospelkaus, A. Pe'er, K. K. Ni, J. J. Zirbel, B. Neyenhuis, S. Kotochigova, P. S. Julienne, J. Ye, and D. S. Jin, Nature Physics **4**, 622 (2008).

[99] J. G. Danzl, E. Haller, M. Gustavsson, M. J. Mark, R. Hart, N. Bouloufa, O. Dulieu, H. Ritsch, and H. C. Nägerl, Science **321**, 1062 (2008).

[100] J. G. Danzl, M. J. Mark, E. Haller, M. Gustavsson, R. Hart, J. Aldegunde, J. M. Hutson, and H. C. Nägerl, Nature Physics **6**, 265 (2010).

[101] P. M. Morse, Phys. Rev. **34**, 57 (1929).

[102] Note that the given dipole moments are taken from MOLPRO standard output which does not include the dipole moment of the core caused by the core polarization potential. We expect deviations in the range of 0.05 D.

[103] B. L. Tolra, N. Hoang, B. T'Jampens, N. Vanhaecke, C. Drag, A. Crubellier, D. Comparat, and P. Pillet, Europhys. Lett. **64**, 171 (2003).

[104] M. Junker, D. Dries, C. Welford, J. Hitchcock, Y. P. Chen, and R. G. Hulet, Phys. Rev. Lett. **101**, 060406 (2008).

[105] P. Pellegrini, M. Gacesa, and R. Cote, Phys. Rev. Lett. **101**, 053201 (2008).

[106] C. M. Dion, C. Drag, O. Dulieu, B. Laburthe Tolra, F. Masnou-Seeuws, and P. Pillet, Phys. Rev. Lett. **86**, 2253 (2001).